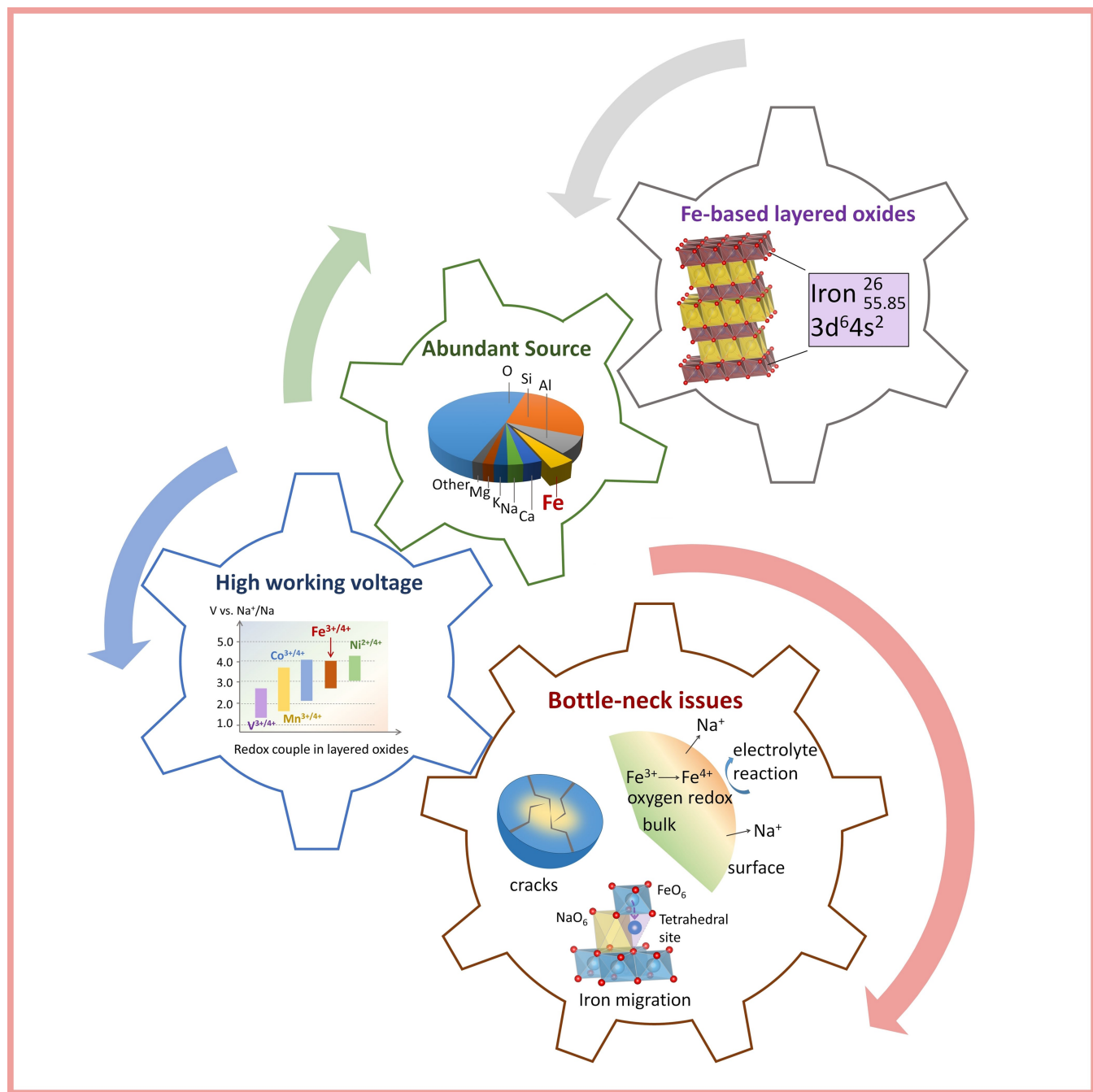


Iron-Based Layered Cathodes for Sodium-Ion Batteries

Xu Gao,^[a] Huanqing Liu,^[a] Wentao Deng,^[a] Ye Tian,^[a] Guoqiang Zou,^[a] Hongshuai Hou,^[a] and Xiaobo Ji^{*[a, b]}



Sodium-ion batteries (SIBs) have grasped renewed attentions in recent years owing to the blooming growth of clean energy and corresponding demands of grid-scale energy storage. Note that, the properties of cathode materials are quite important to the development of SIBs as they largely determine the energy density, cycle life, and cost of a battery. Direct inheriting those Co/Ni based layered cathodes that are successfully utilized in lithium-ion batteries seems to be impractical for SIBs in view of the high materials costs. Fortunately, the discovery of the electrochemical activity of $\text{Fe}^{3+}/\text{Fe}^{4+}$ redox couple in sodium layered materials has opened a new way to design high capacity/voltage and low-cost cathodes for SIBs. To date,

various Fe-based layered oxides have been explored, showing encouraging electrochemical performances in SIBs. However, issues and challenges still remain upon the practical utilization of Fe-based layered cathodes, calling for further targeted and in-depth investigations. In this review, the developing history, key problems, and current progress of Fe-based layered cathodes on electrochemical performances and working mechanism are summarized and discussed. In addition, possible research trends and perspectives are proposed. It is believed that Fe-based layered oxides will be one of the most attractive cathodes for SIBs.

1. Introduction

Originated at the same period of time with lithium-ion batteries (LIBs), sodium-ion batteries (SIBs) have gained much less attention in the past few decades owing to the relatively lower energy density and worse cycling stability.^[1–4] However, along with the booming demands of LIBs in portable devices, electrical vehicles and stationary energy storage, the shortcoming of limited Li/Co source for LIBs has been gradually exposed, reflecting in the increasing material price.^[5,6] Meanwhile, the large-scale energy storage, which plays a crucial role in the ongoing transition from fossil fuels to renewable energy for achieving a greener planet, is asking for rechargeable batteries with high energy density and low cost.^[7,8] In this case, SIBs have grasped renewed interests since 2010s in light of the following potential advantages.^[3,9–12] (I) Similar chemistry with LIBs. As shown in Figure 1(a), a SIB is composed of positive/negative electrodes, separator and electrolyte. Na^+ can be reversibly migrated between cathode and anode during charge and discharge process. The nearly same configuration and working mechanism as LIBs endow SIBs with convenient production thanks to the mature technology. (II) Moderate energy density. Owing to a higher standard electrochemical potential of Na (-2.71 V) than Li (-3.04 V) with respect to SHE as well as the heavier atomic weight, theoretically, the energy densities of SIBs can hardly reach the level of LIBs. However, it should be noticed that SIBs still hold considerable superiority in energy density in comparison with other candidates for large scale energy storage devices such as lead-acid cells. (Figure 1b) Besides, along with the developing of high-capacity cathode materials, it is predictable that the energy density of SIBs could be comparable to that of LiFePO_4/C batteries.^[7,9] (III) High power density. Despite of a larger ionic diameter of Na^+ (1.02 \AA) than Li^+ (0.74 \AA), the energy barriers for Na^+ migration are found to

be lower than that for Li^+ in the layered structures (Figure 1c), potentially leading to the better rate performances with high power densities.^[10,13] (IV) Low cost. Compared with LIBs, the cost advantages of SIBs are mainly featured in materials. For example, Na_2CO_3 is much cheaper than Li_2CO_3 owing to its abundance and none geographical restriction, and the Cu foil current collector used in anode side can be replaced by Al (Figure 1d).^[14]

Despite afore-mentioned merits, the practical utilizations of SIBs still face lots of challenges, among which the major issue comes from the lack of suitable cathode materials that possess high practical energy density, good cycling stability, and low production cost. Similar to LIBs, cathode materials for SIBs can be predominately categorized into transition metal oxides, phosphates, and ferrocyanides.^[2] Their features and recent progresses have been summarized by some reviews.^[10,20–28] No matter in which kind of cathode material, the key elements that majorly determine the electrochemical properties are 3d transition metals (TM).^[29,30] As for LIBs, Ni/Co/Mn based layered oxides together with Fe-based phosphates have shown superior electrochemical properties and have achieved well-known success in practical utilizations.^[31] However, directly adopting Ni/Co based layered compounds as cathodes for SIBs would cause concerns of material costs and sustainability, and Mn-based layered oxides exhibit low working potentials and poor cycling stabilities.^[9,10,32] Sodium vanadium phosphates show high working potential, moderate capacity, and long cycle life, but the rarity of vanadium induce cost concerns as well.^[33,34] In regard of cost-effectiveness, Fe-based cathode materials could be a good choice as Fe is the fourth abundant element in earth crust, even richer than Mn (Figure 1e).^[19,35] As the analogue of LiFePO_4 , NaFePO_4 gained the merited attention. Unfortunately, it prefers to crystallize as the electrochemically inactive marrokite structure rather than the active olivine-type one.^[36] Although the former one has been proved to be active when decreasing the crystallinity or particle size, the low working potential and limited capacity lead to unsatisfied energy density.^[36–38] Other Fe-based materials including fluorophosphates,^[39,40] pyrophosphate,^[41–43] ferrocyanides,^[44–46] and sulfites,^[47,48] have also been explored as cathode materials for SIBs (Figure 1f) based on $\text{Fe}^{2+}/\text{Fe}^{3+}$ redox couple. All these materials display outstanding cycling performances benefited from superior

[a] X. Gao, H. Liu, Dr. W. Deng, Dr. Y. Tian, Prof. G. Zou, Prof. H. Hou, Prof. X. Ji
State Key Laboratory of Powder Metallurgy
College of Chemistry and Chemical Engineering, Central South University
Changsha, 410083, China

[b] Prof. X. Ji
School of Materials Science and Engineering, Zhengzhou University
Zhengzhou, 450000, China.
E-mail: xji@csu.edu.cn

structural stabilities, whereas the major drawbacks lie in limited gravimetric or volumetric energy densities in comparison with layered transition metal oxides (Na_xTMO_2).^[10,21] Apart from all the findings above, another milestone is that $\text{Fe}^{3+}/\text{Fe}^{4+}$ redox couple has been revealed to be electrochemically active in sodium layered oxides, showing high redox potentials over 3.0 V (Figure 1g).^[18,49,50] Such unique electrochemical behaviors that are not found in lithium-based compounds have offered new opportunities to design Co/Ni free and low-cost Fe-based layered cathodes for SIBs.^[49,51–53] After a decade of development, lots of Fe-based or Fe-containing oxides have been proposed, presenting encouraging performances, but some issues and challenges still exist. In this review, the research history, recent progress, future challenges, and perspectives of Fe-based layered cathodes for SIBs are systematically summarized (Figure 2), with the hope of offering references for researchers in related field.

2. Classification of Layered Structure

Typically, the layered structure of Na_xTMO_2 is built up by alternatively ordered stacks of edge sharing TMO_6 octahedral sheets and Na ions sheets. As defined by Delmas in 1980 and widely adopted by subsequent researchers, the stacks of TMO_6/Na^+ layers are categorized into P type and O type in accordance with the surrounding environment of Na ions (P for prismatic and O for octahedral). Furthermore, a specific number (usually 2 or 3) that follows letter P or O is used to describe the unique TMO_6 octahedral sheets within each unit cell, and thus the phase names can be described as P2, P3, O2 and O3 (Figure 3), which are commonly mentioned in literatures. In addition, the prime symbol (') is usually employed to mark the monoclinic distortion of a P type or O type phase, for example, P'3 and O'3.^[54–56]

Generally, O3 and P2 type materials can be easily prepared by controlling the sodium content and reaction conditions. O3 type Na_xTMO_2 , in which the x value is close to 1, can be obtained at moderate temperatures (about 500–800 °C). In this structure, three kinds of TMO_6 slabs (AB, CA, and BC) stack



Xu Gao received his Bachelor (2015) and Master (2018) degree in Materials Science and Engineering at Sichuan University. He is now pursuing his Ph.D. degree at Central South University under the supervision of Prof. Xiaobo Ji. His research focuses on the high-capacity cathode materials for sodium ion battery.



Huanqing Liu is a PhD candidate at College of Chemistry and Chemical Engineering, Central South University. His present research interest is focused on the manganese-based layered oxide materials for sodium ion battery.



Dr. Ye Tian received PhD degree (2017) in condensed physics at Xiangtan University. Now he works as a postdoctoral at Central South University, focus on polyanionic cathode materials for batteries.



Dr. Wentao Deng is currently a research fellow at Central South University, Changsha, China. She received master's degree with the supervision of Prof. Xiaobo Ji at Central South University, and got Ph.D. at University of Bath supervised by Prof. Petra Cameron. Then she undertook postdoc work with Prof. Laurie Peter at University of Bath before joining Central South University as a research fellow.



Dr. Hongshuai Hou is an Associate Professor at the College of Chemistry and Chemical Engineering, Central South University. He received his Ph.D. at Central South University in 2016. His current research interests are electrochemistry and key materials for electrochemical energy storage devices.



Dr. Xiaobo Ji is a "Shenghua" Professor at Central South University and a Fellow of the Royal Society of Chemistry, specializing in the research and development of batteries and supercapacitor materials and their systems. He received his Ph.D. in Electrochemistry in 2007 under the supervision of Prof. Richard Compton at the University of Oxford and undertook postdoctoral work at MIT with Prof. Donald Sadoway.



Guoqiang Zou is an Associate Professor at the College of Chemistry and Chemical Engineering, Central South University. He received his Ph.D. from Central South University in 2018. His current research interests are electrochemistry and key materials for electrochemical energy storage devices.

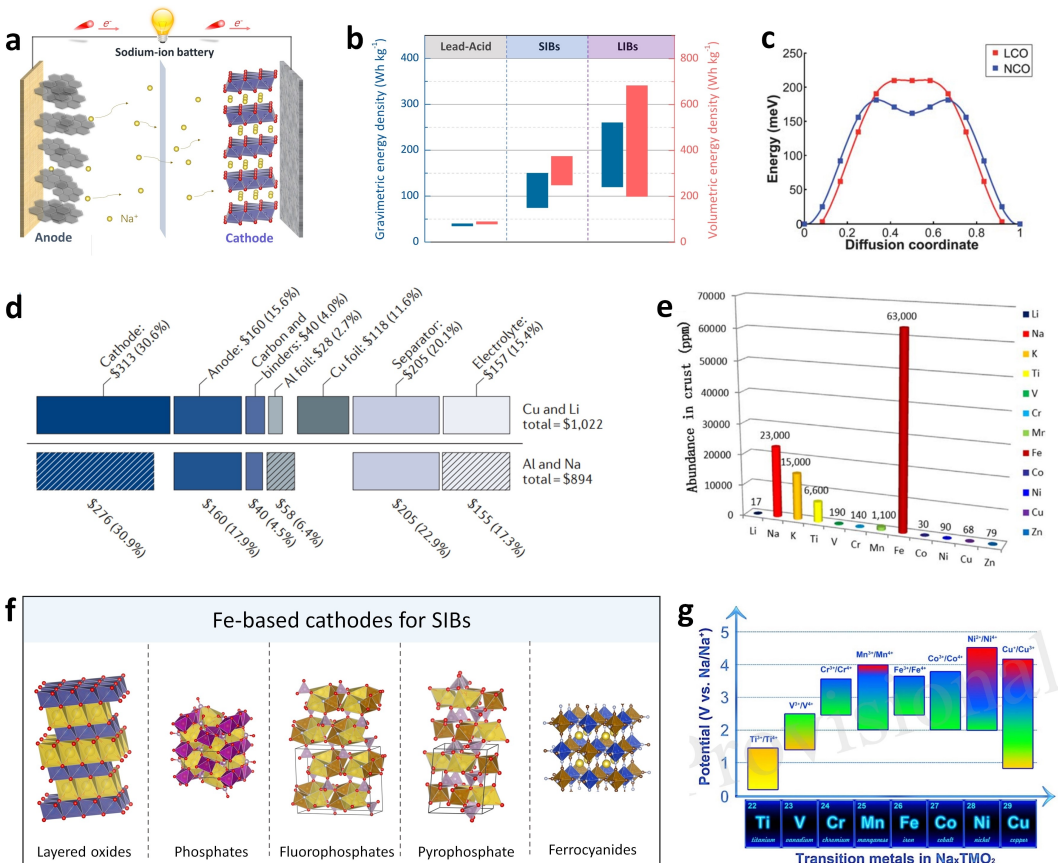


Figure 1. a) Illustration of a sodium-ion battery. b) Comparison of energy density of sodium-ion battery with lead-acid battery and lithium-ion battery. Produced with data in Ref. [15–17]. c) Calculated diffusion barriers for NaCoO₂ and LiCoO₂. Reproduced from Ref. [13] with permission. Copyright (2011) Royal Society of Chemistry. d) Cost and resource analysis of sodium-ion batteries. Reproduced from Ref. [14] with permission. Copyright (2018) Springer Nature. e) Element abundance in Earth's crust. Reproduced from Ref. [19] with permission. Copyright (2017) Elsevier. f) Illustration of typical Fe-based cathode materials for SIBs. g) The redox couples in Na_xTMO₂ compounds with their corresponding potential range. Reproduced from Ref. [18] with permission. Copyright (2019) Elsevier.

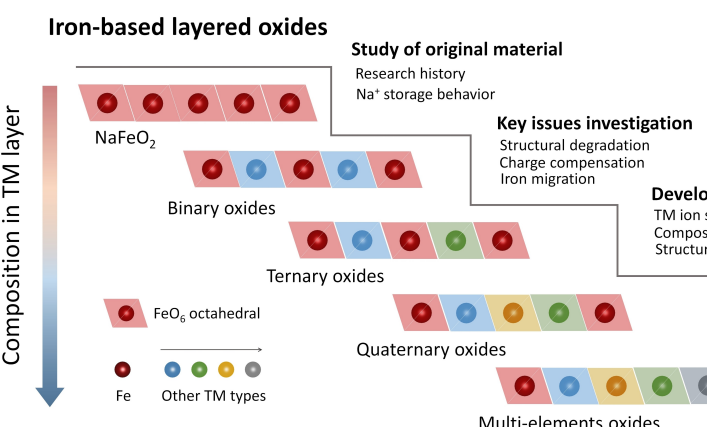


Figure 2. Illustration of iron-based layered oxides and related issues.

repetitively while Na ions occupy the octahedral (O) sites between two adjacent TMO₆ sheets. This cation-ordered rock-salt superstructure is originated from the large ionic radius difference of Na⁺ and transition metal ions. During the electrochemical de-/sodiation process, the pristine O₃ type materials always undergo a series of reversible phase transformations

(O₃↔O'3↔P3↔P'3) along with the gliding of TMO₆ slab because Na⁺ energetically favor prismatic sites after partial extraction of Na⁺.^[10] Notably, the intermediate P3-phase, mainly known to emerge when x≈0.5, can also be prepared directly at specific temperatures. In this structure, TMO₂ layers stack in an order of "AB-BC-CA" and all Na⁺ occupy in prismatic sites that

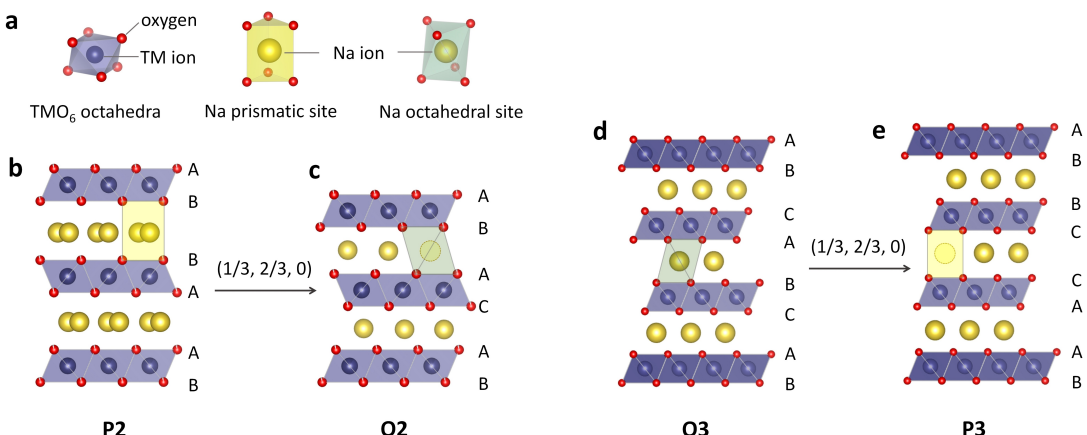


Figure 3. Illustration of typical structures of sodium layered oxides.

share one face with a TMO₆ octahedron and three edges with three TMO₆ octahedra.^[57,58] P2 type Na_xTMO₂ materials, which are stable within a composition range of $0.6 \leq x \leq 0.7$, are prepared at higher temperatures (about 800–1000 °C). In this unique configuration, two kinds of TMO₂ slabs (AB, and BA) heap up alternatively between which Na⁺ occupy the triangular prismatic (P) sites. Notably, these prismatic sites can be divided into two different types: the prisms connecting with two neighboring TMO₆ octahedrons along their faces are denoted as Na_f sites whereas those surrounded by six TMO₆ octahedrons along their edges are denoted as Na_e sites. Benefited from the relatively larger interlayer distance and faster Na⁺ diffusion, P2-type materials normally exhibit better structural stability and electrochemical performance than O3-type ones.^[59,60] However, with a deep extraction of Na⁺, an OP4 (or "Z" phase) or O2 phase may occur due to the glide of TMO₂ layer. Although this P–O phase transition is evidenced to be reversible, the consequent large volume change may cause negative influence upon cycling stability.^[49,61–63]

3. Iron-Based Layered Cathodes for SIBs

3.1. Alpha-NaFeO₂

3.1.1. Discovery History of Electrochemical Activity

α-NaFeO₂ with a typical ordered rock salt structure, which is also known as a prototype of O3-type structure (Figure 4a), was first synthesized by Rousseau and Bernheim in 1888.^[68] In 1985, the chemical desodiation behavior of α-NaFeO₂ was first reported by Kikkawa.^[65] Using bromine as an oxidizing agent, about 10% of sodium was extracted from α-NaFeO₂ together with the observation of Fe⁴⁺ (Figure 4b) in α-Na_{0.9}FeO₂. This is a great finding as it was well-known that the Fe⁴⁺ state only exist in alkaline earth perovskite related compounds such as CaFeO₃ and SrFeO₃. Then in 1994, Takeda et al. successfully examined the electrochemical deintercalation of Na⁺ from α-NaFeO₂ by charging a Li/α-NaFeO₂ cell, further confirming the formation of Fe⁴⁺.^[68] In addition, a monoclinically distorted phase (space

group C2/m) in the desodiated Na_{1-x}FeO₂ ($x \geq 0.2$) appeared, which is attributed to the structural compensation for the loss of Na⁺ in NaO₂ layers. Nevertheless, the reversible (de)sodiation behavior of α-NaFeO₂ had not been revealed until 2006, when Okada and co-workers first reported the charge and discharge capability of α-NaFeO₂ based on Fe³⁺/Fe⁴⁺ redox in a Na/α-NaFeO₂ cell.^[66] Although only a limited reversible capacity (80 mAh g⁻¹) was obtained (Figure 4c), it is a very impressive discovery as the similar behavior was not found for LiFeO₂ in a lithium cell. Nano-sized O3-LiFeO₂ could deliver a reversible capacity of 120 mAh g⁻¹ (Figure 4d), however, it's associated with the Fe²⁺/Fe³⁺ redox and oxygen release.^[67] This is because the 3d-orbital in Fe³⁺ is strongly hybridized with the oxygen 2p orbital in the Li system, hence oxygen removal is more favorable rather than the oxidation of Fe³⁺ to Fe⁴⁺.^[49] In contrast, in the sodium system, the strongly ionized sodium exhibits lower covalency with oxygen, endowing iron and oxygen with more electrons when compared with the lithium system. Consequently, the electrochemical potential of the Fe³⁺/Fe⁴⁺ redox is relatively lower versus Na⁺/Na, making the Fe³⁺/Fe⁴⁺ redox accessible in sodium layered oxides.^[49,69] Notably, along with the development of characteristic technology, more and more accurate evidences supporting the reversible redox of Fe³⁺/Fe⁴⁺ have been obtained by advanced techniques such as electron energy loss spectroscopy (EELS) and X-ray absorption spectroscopy (XAS), which will be discussed in later part.

The unique electrochemical activity of α-NaFeO₂ has greatly inspired the researchers. Yabuuchi systematically examined the electrochemical performances of α-NaFeO₂ in Na/α-NaFeO₂ cells within various voltage ranges.^[64] When the cut-off voltage is limited at 3.4 V, a nearly flat voltage plateau appears at around 3.3 V, resulting in a maximum reversible capacity of 80 mAh g⁻¹ ($x \approx 0.3$ in Na_{1-x}FeO₂) with 75% retention after 30 charge/discharge cycles at a rate of 12 mA g⁻¹ (Figure 4e, f). With the increasing of cut-off voltage, the charging profile tends to be steep meanwhile the reversibility is gradually deteriorated. After charge to 4.5 V, corresponding to 70% sodium extraction, there is almost no reversible discharge capacity. Based on ex-situ XRD results, the irreversible capacity loss was ascribed to the irreversible structural change and the

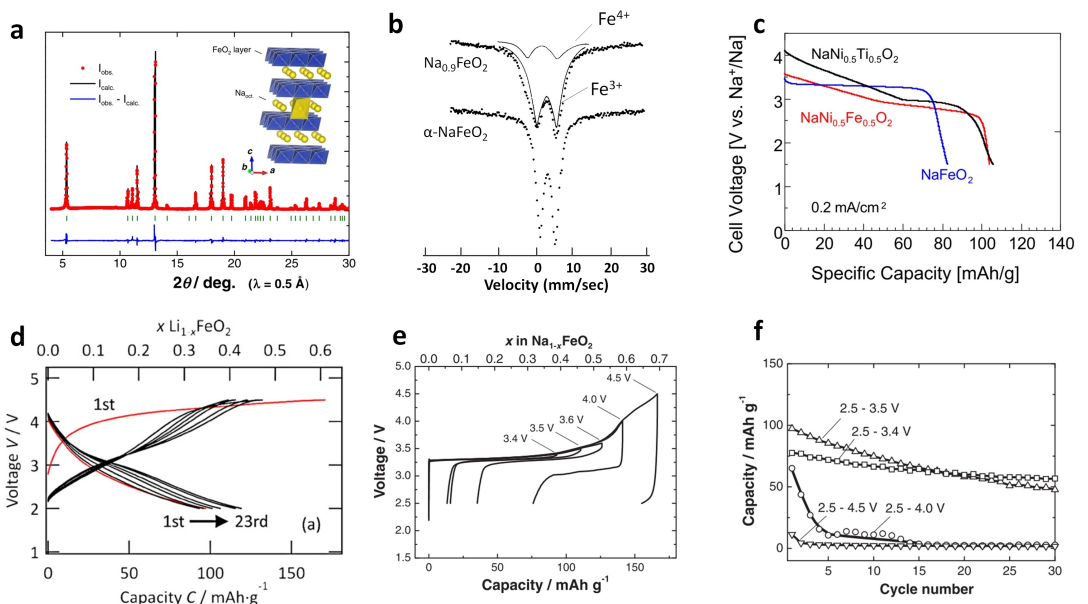


Figure 4. a) XRD pattern and structure illustration of α -NaFeO₂. Reproduced from Ref. [64] with Permissions. Copyright (2012) the Electrochemical Society of Japan. b) Fe Mössbauer spectrum of α -NaFeO₂ and chemically oxidized Na_{0.9}FeO₂. Reproduced from Ref. [65] with Permissions. Copyright (1985) Elsevier. c) Discharge profiles of NaFeO₂, NaNi_{0.5}Fe_{0.5}O₂ and NaNi_{0.5}Ti_{0.5}O₂ cathodes in sodium cell. Reproduced from Ref. [66] with Permissions. Copyright (2006) IOP Publishing. d) Charge/discharge curves LiFeO₂. Reproduced from Ref. [67] with Permissions. Copyright (2011) Elsevier. e) Initial charge/discharge curves of Na/NaFeO₂ cells with different cut-off voltage and f) corresponding capacity retention for 30 cycles (12 mA g⁻¹). Reproduced from Ref. [64] with Permissions. Copyright (2012) the Electrochemical Society of Japan.

possible migration of iron from TM sites (crystallographically denoted as 3a sites) to Na sites (3b or 6c sites), which hinders the intercalation and diffusion of Na ions in the following cycles.

3.1.2. Structural Evolution and Capacity Degradation

Although α -NaFeO₂ is explored as one potential cathode candidate for SIBs based on unique Fe³⁺/Fe⁴⁺ redox couple, it suffers from low reversible capacity and poor cyclic stability. Irreversible structure deterioration is proposed as the major reason by earlier studies, but more detailed information about such structural degradation was not revealed until the utilization of some in-situ measurements. By using in-situ synchrotron X-ray diffraction (SXRD), Lee et al. clearly observed a monoclinic structure (denoted as m -N_{1-x}FO) after extracting \sim 0.4 Na⁺ from NaFeO₂, which is in line with the report by Takeda (Figure 5a).^[70] Furthermore, a sodium deficient topotactic phase (denoted as O'3') that emerges before m -N_{1-x}FO is also identified during charge/discharge process while its asymmetric structural evolution is attributed to the nonequilibrium phase transformation behavior. Such a O'3' - m -N_{1-x}FO phase transition process of α -NaFeO₂ was then verified by Li^[74] and Susanto.^[71] Specially, a new hexagonal structure (denoted as O3''H, Figure 5b) which shows a contracting trend in comparison to O'3' (or denoted as O3'H) phase is also identified after 0.5 Na extraction, which is ascribed to the stacking fault between FeO₆ and NaO₆ slabs. After charging to 4.5 V, only a single monoclinic phase (denoted as O3'm or m -N_{1-x}FO) remains, exhibiting irreversibility in the following discharging process.^[71]

Notably, Silván et al. has reported some different viewpoints in comparison with above-mentioned ones.^[72] By conducting a series of lab-scale in situ powder X-ray diffraction (PXRD) measurements, they claimed that the O3-type NaFeO₂ mainly experiences a uniform solid-solution reaction with the continuous expansion of interlayer (along c axis) distance during desodiation until 30% Na ions are extracted, when a new layered phase starts to appear (Figure 5c). This new phase is identified as monoclinically distorted P3 phase with similar in-plane parameters to the O3 phase, thus it is denoted as a P'3 structure (space group C2/m) (Figure 5d). The distinct results obtained from in-situ PXRD and in-situ SXRD have been ascribed to different configuration of the operando cell because the electrochemical reactions may be strongly delayed in a modified coin cell for in situ SXRD test due to the lower pressure induced by the flexible Kapton windows. However, it is noticed that the in situ PXRD measurement conducted by Li et al. demonstrates a series of two-phase transitions, which is similar with the in situ SXRD results reported by Lee and Susanto (Figure 5e).^[73] Considering these discrepancies, a further confirmation of the structural evolution of O3-NaFeO₂ during (de)sodiation is still needed.

Another factor that may be responsible for the capacity fading of α -NaFeO₂ is the side reactions triggered by Fe⁴⁺ at the electrode-electrolyte interfaces. By examining the quasi-reversibility of α -NaFeO₂ cathode in Na/ α -NaFeO₂ cells,^[70] Lee and co-workers found that the octahedrally coordinated Fe⁴⁺ species generated during desodiation process were chemically unstable since more than 20% of Fe⁴⁺ species are spontaneously reduced back to Fe³⁺ during open circuit storage of the charged cell, according to the ex-situ Mössbauer spectra

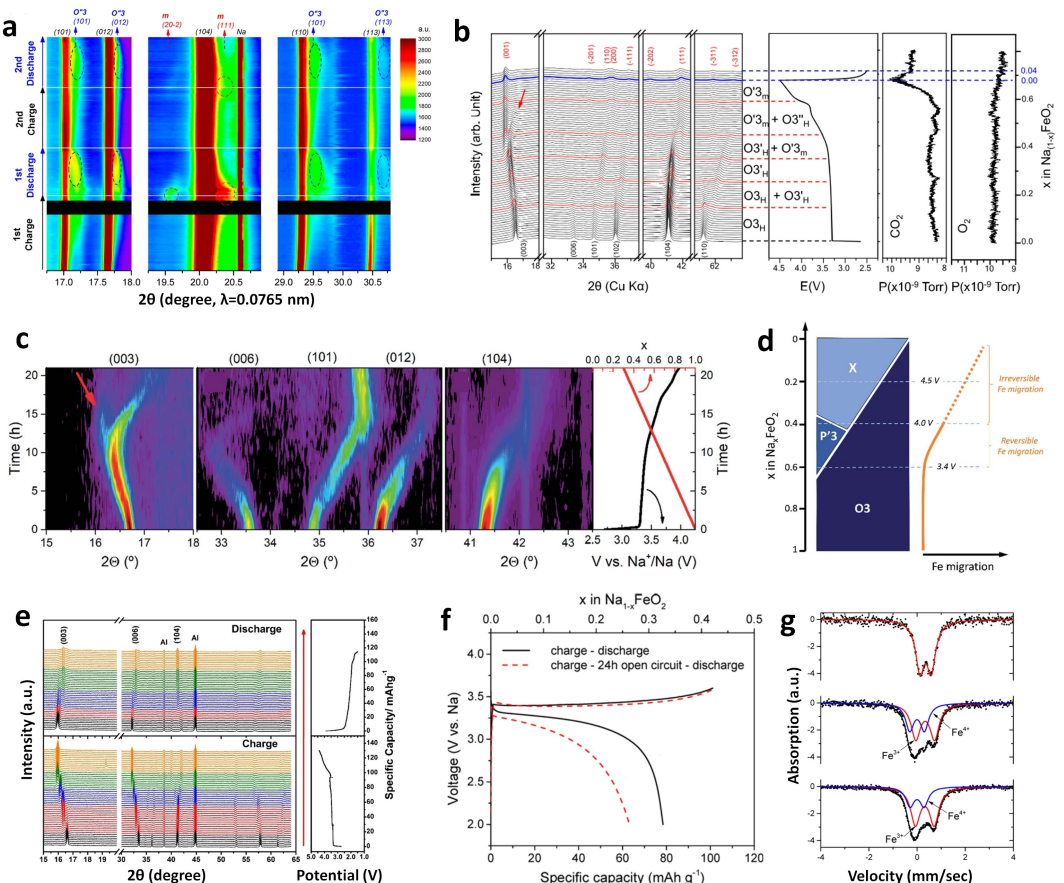


Figure 5. a) In-situ SXRD patterns of NaFeO_2 electrode (contour map) collected at selective 2θ angles during initial cycles. b) In-situ powder XRD measurements and CO_2/O_2 gas evolution for NaFeO_2 conducted by Susanto. Reproduced from Ref. [71] with permissions. Copyright (2019) American Chemical Society. c) In-situ powder XRD results and d) a scheme of phase evolution and iron migration upon sodium extraction in Na_xFeO_2 reported by Silván. e) In-situ powder XRD results for NaFeO_2 reported by Li. Reproduced from Ref. [73] with permission. Copyright (2018) Elsevier. f) Initial voltage profiles of NaFeO_2 (black line: continuous charge-discharge process; red line: a charge-discharge process with a 24 h open circuit period at the state of charge) and g) corresponding Fe Mössbauer spectrum. (a, f, g) Reproduced from Ref. [70] with permissions. Copyright (2015) American Chemical Society. c, d) Reproduced from Ref. [72] with permissions. Copyright (2019) Royal Society of Chemistry.

results (Figure 5f, g). The oxidation of the electrolyte is suggested as the counter reaction accompanied with spontaneous reduction of Fe^{4+} as demonstrated by the electrochemical impedance spectroscopy (EIS) measurements, where an increased interfacial resistance is exhibited during open circuit aging. Although carbonate-based electrolytes are generally thought to be chemically stable at least below 4 V (vs. Na),^[75] it is speculated that the highly oxidative Fe^{4+} could catalyze the oxidation of electrolytes at lower potential. However, more direct evidence is still needed to further prove this viewpoint.

3.1.3. Iron Migration

Note that, with the loss of Na in NaO_6 slabs and sodium/vacancy ordering in 3b sites, the P3-type layered structure is commonly generated in other O3-type NaMO_2 materials like NaCrO_2 ^[76,77] and NaCoO_2 ^[54] via layer gliding, resulting in stepwise voltage change. However, this type of phase transition has not been observed in $\alpha\text{-NaFeO}_2$. Yabuuchi initially

presumed the iron migration from 3a (octahedral sites in TMO_6 layers) to 6c (face-shared tetrahedral sites to 3a sites) and/or 3b (octahedral sites in NaO_6 layers) in view of the irreversible decrease of (003) diffraction peaks in comparison to that of (101) and (104) peaks (Figure 6a).^[35,49,64] In light of the zero octahedral field stabilization energy of Fe^{3+} ions, such type of migration from pristine octahedral sites to the face-shared tetrahedral sites is possible to occur when sufficient sodium vacancies are created as a result of continuous sodium extraction. This hypothesis was then supported by density functional theory (DFT) calculations, which demonstrates that the activation energy for Fe^{3+} migration out of the pristine octahedron sites could be remarkably reduced after a certain amount of Na extraction (Figure 6b). Among several possible pathways, the Fe^{3+} migration from the octahedron sites in FeO_6 layers to their face-shared tetrahedron sites in Na layers is energetically favorable, thus well explaining the driving force and unique orientation of Fe ion migration.^[73] Those Fe ions migrating into sodium layers could not only resist the layer glide through the “pinning effects” but also induce nonuniform sodium extraction by hindering in-plane diffusion of sodium

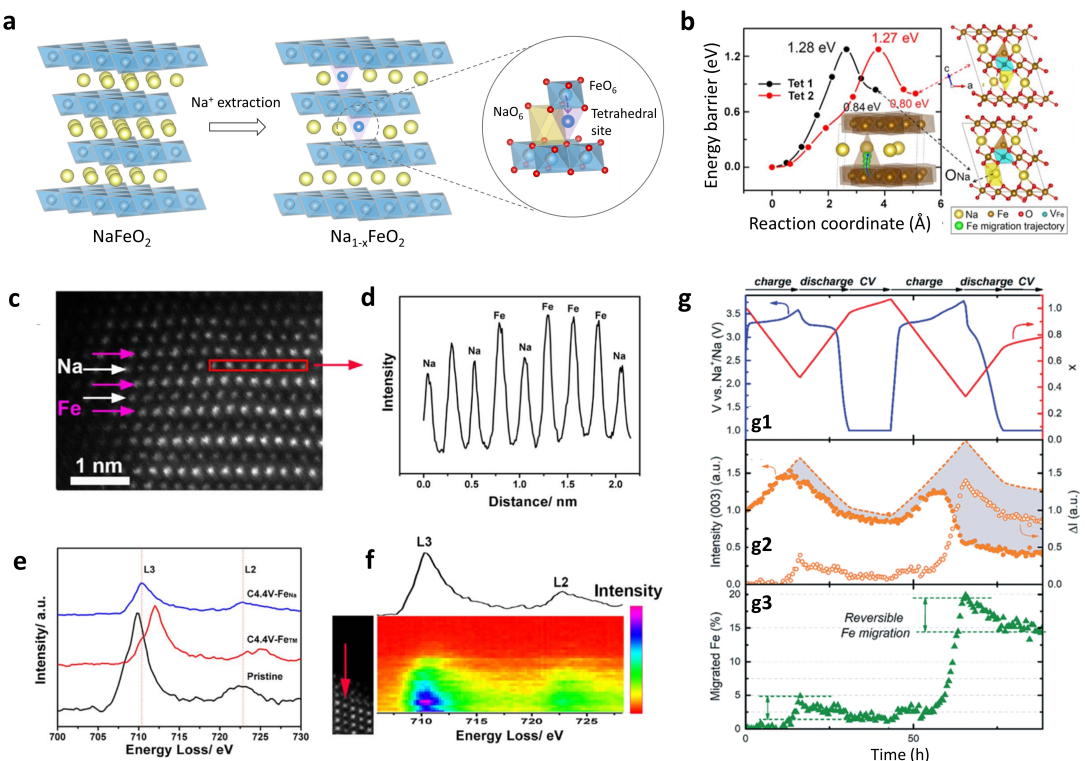


Figure 6. a) Illustration of possible mechanism of the iron migration process during sodium extraction. b) The calculated energy barrier for Fe migration from the transition metal layer to the Na layer in $\text{Na}_{0.33}\text{FeO}_2$. c) HAADF images of NaFeO_2 at the fully charged state, d) corresponding line profile acquired from the red rectangular region, e-f) EELS spectra obtained at different state of charge and f) the contour map of the EELS scanned along the Na layer for full charge NaFeO_2 . b-f) Reprinted from Ref. [73] with permission. Copyright (2018) Elsevier. g) Analysis of the interlayer reflection (003) versus time during the operando PXRD measurement for initial two cycles and calculated Fe migration from Rietveld refinement results. Reproduced from Ref. [72] with permission. Copyright (2018) Royal Society of Chemistry.

ions. This may explain the formation of distorted O3-type phase and/or monoclinic phase instead of P3 phase in desodiated $\text{Na}_{1-x}\text{FeO}_2$.^[70] Then, by using aberration-corrected scanning transmission electron microscopy (STEM), Fe ion migration upon Na extraction in various Fe-based layered oxides was directly observed at the atomic scale.^[73,74,78] In the case of NaFeO_2 , Fe ions occupied in sodium layer are clearly detected by STEM and electron energy loss spectroscopy (EELS) after charging the electrode to 4.4 V (Figure 6c–f). In the following discharge process, the NaFeO_2 phase fails to be fully recovered even after discharging to 1.5 V, indicating the irreversibility or partial irreversibility of Fe^{3+} migration.^[73] Subsequently, Silván and co-workers^[72] pointed out that iron migration in $\text{Na}_{1-x}\text{FeO}_2$ most probably occurred when $x \geq 0.5$, hereupon suppressing the O3-P3 phase transition and inducing the contraction of O3 phase. After charging to 4.0 V, about 40% of the initial iron ions would be migrated according to the quantitative calculation of the intensity loss of (003) reflection. Moreover, a partial reversibility of the iron migration at the cost of a high over-polarization is detected by in situ PXRD and PITT measurements (Figure 6g). The same phenomenon has also been observed in other Fe-based layered cathodes, and it will be introduced in later part.

As a short summary, the migration of Fe ions from TM layer to sodium layer in O3- NaFeO_2 has been widely demonstrated. Such migration of Fe is reckoned as the major factor causing

the capacity fading of O3- NaFeO_2 during (de)sodiation process due to the hindered sodium diffusion, non-equilibrium sodium extraction, and the nucleation of irreversible phase. In regarding that Fe ions are more apt to migrate than other 3d ions like Ni, Co, and Mn in sodium transition metal oxides, one reason may be the energy favorable nature of trivalent Fe in tetrahedral sites. Moreover, the strong Jahn-Teller distortion of a neighboring Fe^{4+}O_6 octahedron may facilitate the migration of Fe as it can accommodate the shrink of the tetrahedron with a migrating Fe.^[74] In other word, Fe migration tends to occur in O-type stacking when too much Fe is clustering and the oxidation of $\text{Fe}^{3+}/\text{Fe}^{4+}$ is accessible. These findings greatly inspired the following exploration of Fe-based materials which will be discussed in later section.

3.1.4. Anionic Redox Behavior

As known, some Fe^{4+} -contained materials like CaFeO_3 and SrFeO_3 possess the electronic structure of $3d^5L$ rather than $3d^4$, in which the “L” represents a ligand hole from oxygen, indicating the preferential activity of oxygen over iron.^[79] In regard of O3-type LiFeO_2 , the oxygen evolution is recognized to be more favorable than the oxidation of Fe^{3+} due to the strongly hybridization of Fe^{3+} 3d-orbital with oxygen 2p orbital.^[49,68] However, the oxygen evolution in O3- NaFeO_2 was

once ignored possibly due to the consideration that Fe^{3+} has less hybridization with oxygen in sodium system.^[49] Li with co-workers initially reported the oxygen oxidation behavior during Na extraction from NaFeO_2 .^[73] Based on ex situ X-ray photoelectron spectroscopy (XPS) and X-ray absorption spectroscopy (XAS) measurements, they found that, beyond Fe^{3+} oxidation, the $(\text{O}_2)^{\text{n}-}$ species and $\text{O}_{2\text{p}}\text{-TM}_{3\text{d}}$ hybridized states which indicate the oxygen evolution occurred after charging to 3.4 V and even become dominant as the charge process continues (Figure 7a, b). In the following discharge process, the oxygen evolution exhibits a good reversibility. In addition, the migration of iron is reckoned as the trigger for oxygen oxidation since it may intensify the structural distortion and locally weaken the Fe–O interaction. More recently, Susanto et al. claimed a new viewpoint that the oxygen evolution might occur at the beginning of charging, followed by the gradual formation of Fe_3O_4 upon the deep desodiation process.^[71] According to the detailed near-edge X-ray absorption fine structure (NEXAFS) measurements (Figure 7c–e), the pre-edge peak at around 528 eV, marked with A) emerging from the beginning of Na extraction

demonstrates the $3\text{d}^5\text{L}$ structure of Fe^{4+} while the shape evolution of peak B ($t_{2g}\text{L}$) and C ($e_g\text{L}$) corresponded to Fe 3d–O 2p hybridization. The increased intensity of peak A in the range of $0 < x < 0.4$ in $\text{Na}_{1-x}\text{FeO}_2$ is attributed to the redox activity of oxygen, and the attenuation of peak A in the range $x > 0.5$ is ascribed to oxygen release. Gas evolution was also investigated during in-situ XRD test, as shown in Figure 5(b), but no O_2 evolution has been detected. Instead, evolution of CO_2 gas is observed after 0.57 Na is extracted, which is attributed to the possible immediate reaction between the released O_2 and electrolyte. However, more evidences are still needed to clarify the formation of CO_2 as it may also come from the reaction between Fe^{4+} and the electrolyte.^[70] In addition, the formation of Fe_3O_4 on the surface of $\text{Na}_{0.33}\text{FeO}_2$ particle (charged to 4.5 V), which is considered as the product of oxygen release, is confirmed by selected-area electron diffraction (SAED) and electron energy loss spectroscopy (EELS) (Figure 7f–l). Therefore, the Fe_3O_4 layer formed on the surface of $\text{Na}_{1-x}\text{FeO}_2$ ($x > 0.5$) particle is thought to be responsible for the capacity degradation as it may block the further Na intercalation (Figure 7m).

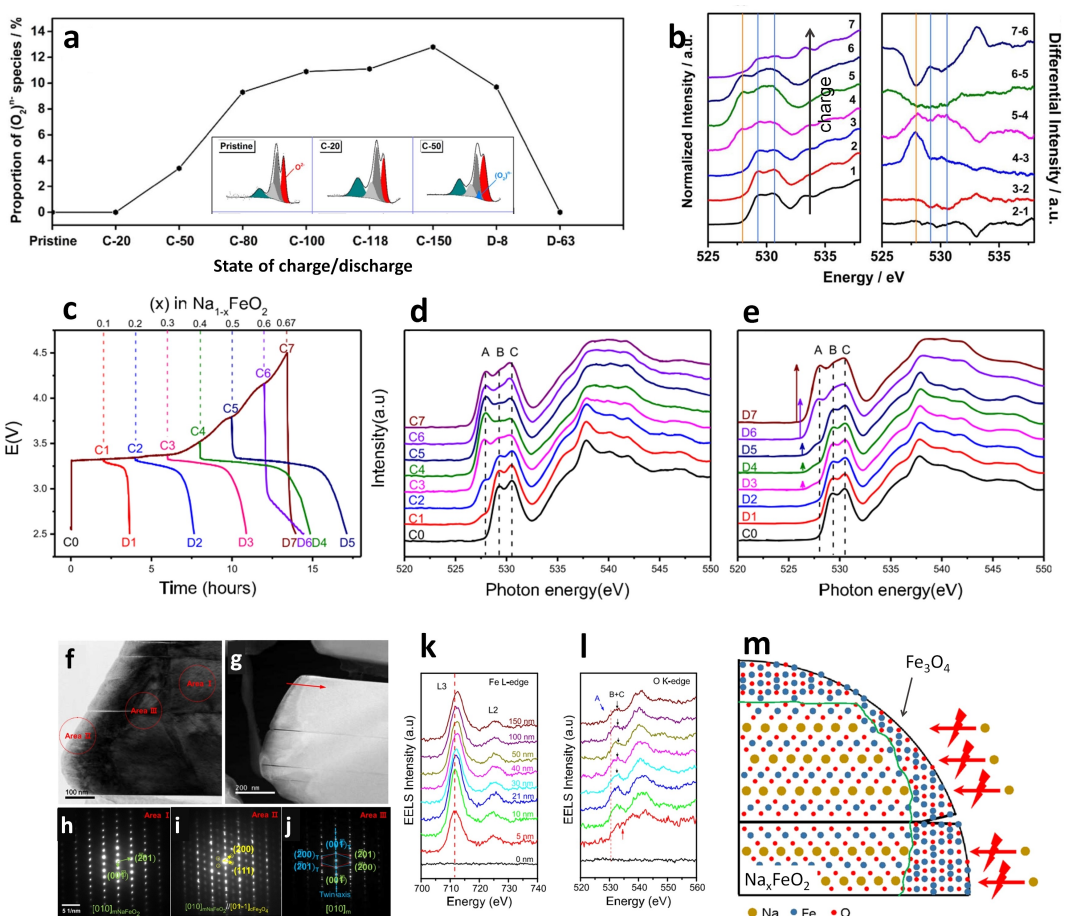


Figure 7. a) The fraction of lattice oxygen of the $(\text{O}_2)^{\text{n}-}$ species at various charge/discharge states obtained from XPS spectra (partially shown in inset) of O1s for NaFeO_2 . b) The O K-edge of NaFeO_2 under the FY mode at different charge states (left) and the differential of the two adjacent spectra (right). a, b) Reproduced from Ref. [73] with permission. Copyright (2018) Elsevier. c) Charge-discharge profile of NaFeO_2 at 0.05 C, and d, e) O K-edge XAS spectra in fluorescence yield (FY) mode collected at different state of charge as marked in (c). f, g) Representative microstructure of $\text{Na}_{1-x}\text{FeO}_2$ samples after charging to 4.5 V observed by f) BF TEM, g) HAADF STEM, and h–j) SAED. k) Fe L-edge and l) O K-edge EELS collected from the surface (bottom) to the bulk (top) along the arrow shown in (g). m) Schematic illustration of irreversible Na insertion into $\text{Na}_{1-x}\text{FeO}_2$ after charging to 4.5 V. c–m) Reproduced from Ref. [71] with permission. Copyright (2019) American Chemical Society.

3.2. Binary $\text{Na}_x[\text{Fe}_y\text{Me}_{1-y}]\text{O}_2$ ($0 < x \leq 1$, $0 < y < 1$)

The electrochemical performances of O3-NaFeO₂ as the cathode of SIB are predominantly constrained by the inherent problems such as iron migration, irreversible phase transition, and oxygen release, which can hardly be solved by conventional surface or morphology modification strategy. In this case, metal substitution is expected to be the most effective way to settle the matters. To date, various metals like Mn, Ni, Co, and Ru, et al. have been utilized to partially replace Fe, successfully improving the electrochemical performance of Fe-based layered cathodes.^[35,80,81]

3.2.1. $\text{Na}_x[\text{Fe}_y\text{Mn}_{1-y}]\text{O}_2$ ($0 < x \leq 1$, $0 < y < 1$)

Manganese, as one of the earth-abundant elements only next to iron in crust, has been widely used in energy storage materials owing to its rich oxidation states (+2/+3/+4) and good electrochemical activity.^[82] A series of $\text{Na}_x[\text{Fe}_{1/2}\text{Mn}_{1/2}]\text{O}_2$ cathodes for SIBs were reported by Yabuuchi and co-workers

for the first time in 2012.^[49] Notably, the initial motivation of this work is to design a P2 type Na_xFeO_2 as P2-type materials generally exhibit higher reversible capacity than O3-type ones owing to the lower barriers for ion diffusion and better structural stability in a wide composition range. However, this idea failed to materialize as Fe^{4+} species can hardly be stabilized in the oxygen framework under ambient conditions. Through the substitution of 50% Fe with Mn, which compensates the loss of Na^+ by oxidizing the same amount of Mn^{3+} to Mn^{4+} , the P2-type $\text{Na}_{2/3}[\text{Fe}_{1/2}\text{Mn}_{1/2}]\text{O}_2$ was successfully obtained. Tested in the half cell with sodium metal anode, P2- $\text{Na}_{2/3}[\text{Fe}_{1/2}\text{Mn}_{1/2}]\text{O}_2$ cathode delivers a high reversible capacity of 190 mAh g⁻¹ (~72% of the theoretical capacity) in the voltage window of 1.5–4.3 V. This capacity is much higher than that of the pristine O3-NaFeO₂ (< 100 mAh g⁻¹). (Figure 8a) With an average working potential of 2.74 V, an ultra-high energy density of 520 Wh kg⁻¹ can be achieved, which is comparable to that of LiFePO₄ cathode for LIBs. The galvanostatic charge/discharge curves of Na/P2- $\text{Na}_{2/3}[\text{Fe}_{1/2}\text{Mn}_{1/2}]\text{O}_2$ cell clearly show two couples of voltage plateaus at around 2.2/2.4 V and 3.4/4.0 V, indicating the participation of both $\text{Mn}^{3+}/\text{Mn}^{4+}$ and Fe^{3+}

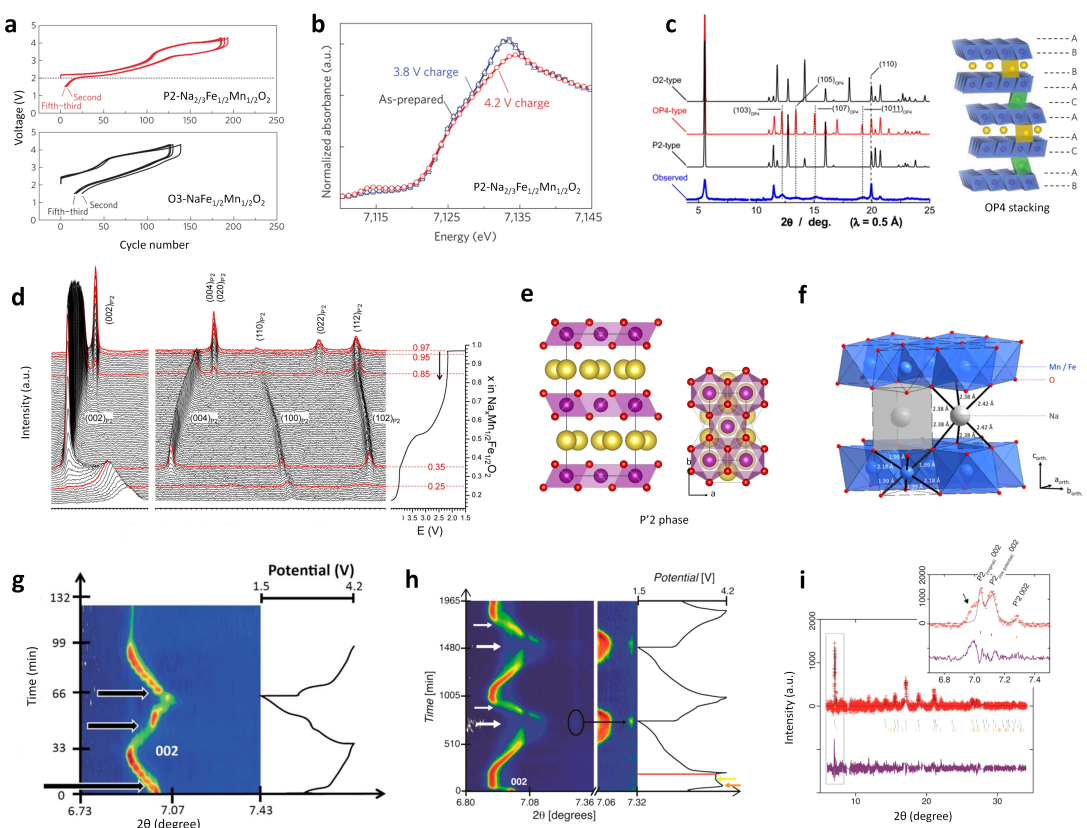


Figure 8. a) Galvanostatic charge/discharge curves for $\text{Na}/\text{Na}_{2/3}[\text{Fe}_{1/2}\text{Mn}_{1/2}]\text{O}_2$ and $\text{Na}/[\text{Fe}_{1/2}\text{Mn}_{1/2}]\text{O}_2$ cells tested at 12 mAh g⁻¹ within 1.5–4.3 V. b) Fe K-edge XANES for $\text{Na}_{2/3}[\text{Fe}_{1/2}\text{Mn}_{1/2}]\text{O}_2$ at different state of charge. c) Simulated XRD patterns for P2-type $\text{Na}_x[\text{Fe}_{1/2}\text{Mn}_{1/2}]\text{O}_2$ samples charged to 4.2 V and a proposed schematic illustration of OP4-type stacking. Reproduced from Ref. [49] with permission. Copyright (2012) Springer Nature. d) In situ XRD patterns of the P2-type $\text{Na}_x\text{Mn}_{1/2}\text{Fe}_{1/2}\text{O}_2$ electrode material during charging within 1.5–4.3 V. e) Illustration of P'2 structure. f) Representation of the MO_6 and NaO_6 polyhedra in the P'2- $\text{NaMn}_{1/2}\text{Fe}_{1/2}\text{O}_2$ phase: highlighting of the cooperative Jahn-Teller effect. d–f) Reproduced from Ref. [89] with permission. Copyright (2014) American Chemical Society. g) Selected 2θ regions of in-situ SXRD data (tested at 1 C-rate) highlighting the evolution of the (002) diffraction peak of P2- $\text{Na}_{2/3}[\text{Fe}_{1/2}\text{Mn}_{1/2}]\text{O}_2$. Reproduced from Ref. [90] with permission. Copyright (2015) Royal Society of Chemistry. h) Selected 2θ regions of in-situ SXRD data highlighting the evolution of the (002) diffraction peak of P2- $\text{Na}_{2/3}[\text{Fe}_{0.4}\text{Mn}_{0.6}]\text{O}_2$, and i) Rietveld refined fit of P2_(original), P2_(low potential), and P2 models to the in-situ SXRD data set closest to the discharged state, $\text{Na}_{0.57(8)}\text{Fe}_{0.4}\text{Mn}_{0.6}\text{O}_2$. h, i) Reproduced from Ref. [91] with permission. Copyright (2015) American Chemical Society.

/Fe⁴⁺ redox which is further evidenced by ex situ XAS (Figure 8b).^[83] However, the cyclic stability of P2-Na_{2/3}[Fe_{1/2}Mn_{1/2}]O₂ is not satisfied as only about 80% of the initial capacity remains after 30 cycles. O3-type Na[Fe_{1/2}Mn_{1/2}]O₂ was also synthesized for comparison, exhibiting much less reversible capacity (100–110 mAh g⁻¹) and larger polarization than that of P2-Na_{2/3}[Fe_{1/2}Mn_{1/2}]O₂.

The ultra-high capacity of P2-Na_{2/3}[Fe_{1/2}Mn_{1/2}]O₂ can be mainly attributed to the good reversibility of Mn³⁺/Mn⁴⁺ and Fe³⁺/Fe⁴⁺ redox and the sufficient Na vacancies in P2-type configuration which allows extra Na⁺ insertion beyond the initial stoichiometric. However, in the case of full cells, the sodium deficiency in P2-Na_{2/3}[Fe_{1/2}Mn_{1/2}]O₂ would be a serious issue as the initial capacity is limited. Further increasing the Na content in P2-type Na_x[Fe_{1/2}Mn_{1/2}]O₂ has been found to be impracticable as O3-type structure preferred to form when x is higher than 0.71.^[84,85] By contrast, adding sacrificial agents as extra Na source seems to be a more feasible strategy. For example, the irreversible capacity of P2-Na_{2/3}[Fe_{1/2}Mn_{1/2}]O₂ in the first cycle can be reduced from 59 mAh g⁻¹ to 27 mAh g⁻¹ by adding 5 wt% NaN₃ as a sacrificial salt.^[86] Very recently, other sacrificial agents such as diethylenediamine penta-acetic acid salt and Na₂C₂O₄ have also been proved to be effective in compensating the sodium deficiency of P2-type materials.^[87,88]

In view of the unsatisfied cycling stability of P2-Na_{2/3}[Fe_{1/2}Mn_{1/2}]O₂, much efforts have been made on disclosing its structural evolution during (de)sodiation process. According to the ex situ XRD results, Yabuuchi proposed that P2-Na_{2/3}[Fe_{1/2}Mn_{1/2}]O₂ prefers to form an OP4-type stacking (Figure 8c) in high charge states (4.2 V) on the basis of structural simulation, differing from typical P2-Na_x[Ni_{1/3}Mn_{2/3}]O₂ that normally undergoes a P2-O2 phase transition after charging above 4.1 V.^[63] Such an OP4 stacking is deemed as an intermediate configuration in between P2-O2 phase transition, originated from the selectively Na⁺ extraction from one out of two layers. Subsequently, the in-situ XRD measurements performed by Boisse and Singh et al. clearly reveal that a new peak emerges at around 17° when charging over 4.0 V (corresponds to x < 0.35 in Na_xFe_{0.5}Mn_{0.5}O₂) and then shifts to higher 20 angle when further charging to 4.3 V. Meanwhile, (002), (004), and (102) diffraction peaks of P2 phase are gradually vanished, indicating the formation of a new phase.^[89,92] (Figure 8d) Note that, Singh et al. attributed this new structure to OP4 phase in accordance with the description of Yabuuchi, while Boisse et al. denoted it as a "Z" phase since the broadening peaks are hardly to be indexed. This structural change has also been evidenced by in situ Raman spectra in consideration of the disappeared E_{2g} mode at 569 cm⁻¹.^[92] Moreover, another new phase, which can hardly be indexed to the pristine P6₃/mmc space group symmetry according to both XRD and Raman results, is detected when x in Na_xFe_{0.5}Mn_{0.5}O₂ is higher than 0.85 during discharging. Finally, this structure is defined as a P'2 phase with orthorhombic distortion as it matches well with the features of P'2- Na_{0.7}MnO₂ (Figure 8e).^[93] Notably, the Rietveld refinement further shows that the cooperative Jahn-Teller effect is the driving force of this transition and the Na⁺ ions are much less mobile for a stoichiometry close to NaFe_{0.5}Mn_{0.5}O₂ (Figure 8f).

Another fact given by the *in situ* XRD and Raman analysis is that both P2-OP4 and P2-P'2 phase transition are of good reversibility. Therefore, it suggests that the structural transitions have few effects on the short-term cycling of the material.^[89] However, the considerable volume change through the whole process of P'2-P2-OP4 transition may have non-negligible effects on the cycling stability, especially in a long-term operation. By limiting the voltage window within narrow ranges so as to evade the formation of OP4 and/or P'2 structure and retain a simple solid-solution reaction of P2 phase, the cycling stability of P2-Na_{2/3}[Fe_{1/2}Mn_{1/2}]O₂ can be significantly improved although at the cost of capacity in initial cycles.^[94] Aim at enhancing the cycling stability without sacrificing the capacity, other strategies such as downsizing the particle size to shorten the ion diffusion pathway or compositing with carbonaceous materials to facilitate electron transfer rate has been explored.^[95–98] These methods show positive effects on cycling stability within short-term cycles whereas an observation of long-term cycling performance is still needed.

P2-Na_{2/3}[Fe_{1/2}Mn_{1/2}]O₂ is a typical prototype of Fe–Mn based layered materials, in which the Fe/Mn ratio is 1:1. Notably, materials with different Fe/Mn ratio have also been prepared and investigated. With the hope of further elevating energy density, the proportion of Fe is increased to 2/3 to obtain P2-Na_{2/3}Fe_{2/3}Mn_{1/3}O₂.^[99,100] This material delivers a capacity of 151.1 mAh g⁻¹ during the 1st discharge within 4.2–1.5 V, followed by rapid capacity fading even though the P'2 phase is not detected in fully discharged state (1.5 V). By employing modified heating process, the initial capacity can be further raised, while the severe capacity fading still exist. Besides, although containing more Fe, P2-Na_{2/3}Fe_{2/3}Mn_{1/3}O₂ exhibits an average discharge voltage of to be 2.74 V, which shows no improvements in comparison with that of P2-Na_{2/3}[Fe_{1/2}Mn_{1/2}]O₂. Thus, the energy density is decreased. Sharma et al further investigated the current rate dependence of the structural evolution of P2-Na_{2/3}[Fe_{2/3}Mn_{1/3}]O₂.^[90] They found that the OP4/"Z" phase is not formed in the charged state when cycled at 1 C unless allowing sufficient rest from the charged state after cycling at 1 C (Figure 8g). It's easy to understand the absence of OP4/"Z" phase when cycled at 1 C as the Na concentration may not be reduced to lower than 0.33, but the OP4-like phase appears during high rate cycling/relaxation, which suggests that the bulk Na content is not necessarily the critical driver for this transformation. However, more detailed investigations may still be needed to further explain this interesting phenomenon. In contrast, increasing the fraction of Mn, for example P2-Na_{0.67}Fe_{0.4}Mn_{0.6}O₂, surprisingly stabilizes the P2 structure in the charged state since OP4/"Z" phase has not been found after charging to 4.2 V even at a current rate of 1/10 C.^[91] In spite of this, the P2-Na_{0.67}Fe_{0.4}Mn_{0.6}O₂ still suffer from dramatic capacity deterioration within initial 20 cycles. Meanwhile, the reversible capacity and average voltage are all decreased when compared with P2-Na_{2/3}Fe_{1/2}Mn_{1/2}O₂ and P2-Na_{2/3}Fe_{2/3}Mn_{1/3}O₂. Note that, a two-phase region (P₂_{original} and P₂_{new} phase) and a three-phase region (P₂_{original}, P₂_{low potential} and P'2 phase) are observed during charging and discharging process, respectively (Figure 8h, i). As such a multi-phase behavior has not been noticed for P2-Na_{2/3}Fe_{2/3}Mn_{1/3}O₂.

$\text{Na}_3[\text{Fe}_{1/2}\text{Mn}_{1/2}]\text{O}_2$, it is speculated that Fe/Mn ratio may play an important role in affecting the structural evolution during Na insertion/extraction while more detailed investigations are still required.

Owing to less reversible capacity and lower average voltage, O3-type $\text{Na}_x[\text{FeMn}]\text{O}_2$ materials have gained much fewer attentions than P2-type ones. Actually, $\text{NaFe}_{1/2}\text{Mn}_{1/2}\text{O}_2$ is hardly prepared as pure O3-type structure, in which a small amount of undefined impurity phases is generally found (Figure 9a).^[49,101] In our view, this may be ascribed to the high concentration of Mn³⁺ ions in the pristine materials, which cause severe structural distortion due to Jahn-Teller effects just as what occurs in both P2-type $\text{Na}_{0.7}\text{MnO}_2$ and O'3-type NaMnO_2 . These effects may also be partially responsible for the poor electrochemical performances of $\text{NaFe}_{1/2}\text{Mn}_{1/2}\text{O}_2$ in consideration of the sluggish Na⁺ diffusion. Designing sodium-deficient O3-type $\text{Na}_x[\text{FeMn}]\text{O}_2$ with less Mn³⁺ and larger interlayer spacing is proposed to be a feasible way to overcome the above-mentioned issues. Han and co-workers successfully obtained an O3-type $\text{Na}_{2/3}\text{Fe}_{1/2}\text{Mn}_{1/2}\text{O}_2$ material by carefully controlling the synthesis method.^[102] Interestingly, O3-type $\text{Na}_{2/3}\text{Fe}_{1/2}\text{Mn}_{1/2}\text{O}_2$ shows comparable electrochemical performances with P2-type $\text{Na}_{2/3}\text{Fe}_{1/2}\text{Mn}_{1/2}\text{O}_2$. They also prepared an O3-type $\text{Na}_{2/3}\text{Fe}_{2/3}\text{Mn}_{1/3}\text{O}_2$, observing similar electrochemical performances with that of P2-type $\text{Na}_{2/3}\text{Fe}_{2/3}\text{Mn}_{1/3}\text{O}_2$ except for a littler

lower working potential (Figure 9b, c).^[99,103] Hence, it is suggested that the Na⁺ concentration of pristine state may influence the overall electrochemical performances more than the crystallographic phase. In addition, on the basis of the same composition of O3-type $\text{Na}_{2/3}\text{Fe}_{2/3}\text{Mn}_{1/3}\text{O}_2$ and P2- $\text{Na}_{2/3}\text{Fe}_{2/3}\text{Mn}_{1/3}\text{O}_2$, Katcho and co-workers further investigated the relative stability and Na⁺ mobility in these two compounds through Density Functional Theory (DFT) calculation and experimental studies (Figure 9d-i).^[60] One conclusion is that the electrostatic energies of P2 and O3 phases are quite close in spite of the different interlayer distances between MO₆ sheets, leading to parallel stability of these two compounds. Moreover, their results also show a higher Na⁺ diffusion coefficient for P2 phase than O3 phase, indicating the superiority of P2-type materials in designing state-of-the-art cathodes for SIBs.

3.2.2. $\text{Na}_x[\text{Fe}_{y}\text{Ni}_{1-y}]\text{O}_2/\text{Na}_x[\text{Fe}_{y}\text{Co}_{1-y}]\text{O}_2$ ($0 < x \leq 1$, $0 < y < 1$)

As known, NaCoO_2 and NaNiO_2 are all recognized as promising cathodes for SIBs owing to the good electrochemical activity of Co^{3+/4+} and Ni^{3+/4+} redox.^[104,105] With the hope of suppressing iron migration and irreversible phase transition of O3- NaFeO_2 , Co³⁺ and Ni³⁺ have been utilized to substitute partial Fe³⁺. Notably, Yoshida et al. replaced 50% of Fe in O3- NaFeO_2 with

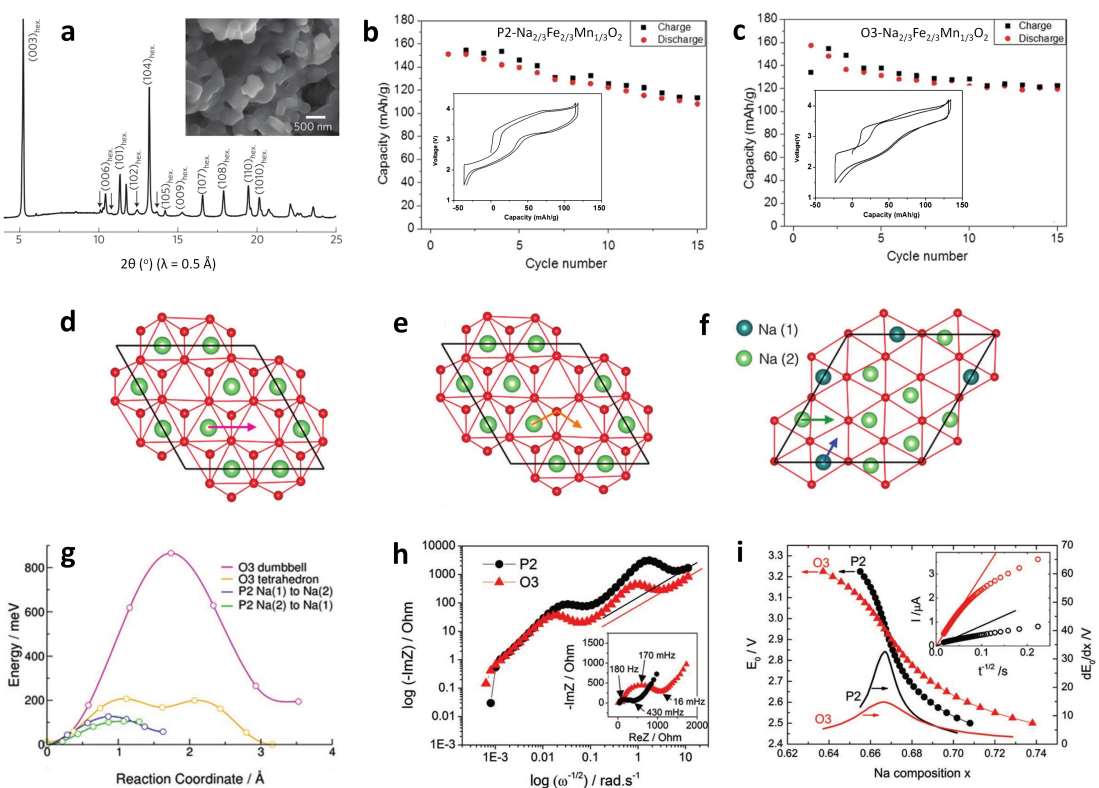


Figure 9. a) XRD pattern and SEM image of O3- $\text{NaFe}_{1/2}\text{Mn}_{1/2}\text{O}_2$. Reproduced from Ref. [49] with permission. Copyright (2012) Springer Nature. Charge/discharge curves and cycling performances of b) P2- $\text{Na}_{2/3}\text{Fe}_{2/3}\text{Mn}_{1/3}\text{O}_2$ and c) O3- $\text{Na}_{2/3}\text{Fe}_{2/3}\text{Mn}_{1/3}\text{O}_2$. Reproduced from Ref. [99] with permission. Copyright (2014) Royal Society of Chemistry. d–g) Computed diffusion paths and energy profiles using DFT: d) O3 dumbbell hop, e) O3 tetrahedral hop, f) Na(1) to Na(2) and Na(2) to Na(1) P2 hops, and g) energy profiles for the diffusion paths depicted in (d–f). h) Imaginary part of the complex impedance measured from EIS as a function of $\omega^{-1/2}$ in log-log scale for half cells of the P2 and O3 phases. i) Equilibrium voltage and its derivative as extracted from the PITT measurements of half cells of the P2 and O3 phases. d–i) Reproduced from Ref. [60] with permission. Copyright (2017) Wiley-VCH.

Co, obtaining $\text{NaCo}_{0.5}\text{Fe}_{0.5}\text{O}_2$.^[51] The introduction of Co surprisingly eliminates the formation of any irreversible phase during charging process. Reversible Na extraction occurs in a wide composition range from NaFeO_2 to $\text{Na}_{0.3}\text{FeO}_2$ (tested within 4.0–2.5 V), bringing a high capacity of 160 mAh g^{-1} , which is even higher than that of NaCoO_2 (tested within 4.0–2.0 V). Additionally, about 85% of the initial capacity can be retained after 50 cycles, indicating a much better cycling stability than that of NaFeO_2 (Figure 10a, b). More impressively, an excellent rate capability is achieved, as a discharge capacity over 100 mAh g^{-1} can be gained at 30 C rate (7.23 A g^{-1}), which is attributed to the simplified phase transition behavior in comparison with that of NaCoO_2 and the fast sodium diffusivity in the P3 phase. Afterwards, they further investigated the structural and electrochemical properties of a series of $\text{NaFeO}_2\text{-NaCoO}_2$ solid solution by means of X-ray and neutron diffraction (ND) analysis. The in-situ powder XRD results clearly reveal the O3-P3-P'3-O3' phase transition of $\text{Na}_{1-x}\text{Fe}_{0.5}\text{Co}_{0.5}\text{O}_2$

during charging process, which is distinct from that of both $\text{Na}_{1-x}\text{FeO}_2$ and $\text{Na}_{1-x}\text{CoO}_2$ (Figure 10c). Although transition metal (Fe/Co) ordering do not occur in all the samples as proved by ND measurements and theoretical calculation/simulation (Figure 10d), $\text{Na}^+/\text{vacancy}$ ordering of $\text{Na}_{0.5}\text{Fe}_{0.5}\text{Co}_{0.5}\text{O}_2$ is detected by ex-situ SXRD, which explains the correspondingly sudden voltage jump (Figure 10e, f). Moreover, the calculated Bader charges together with ex-situ XANES results further verify the participation of both $\text{Fe}^{3+}/\text{Fe}^{4+}$ and $\text{Co}^{3+}/\text{Co}^{4+}$ redox in charge compensation upon Na^+ extraction/embedding.

Wang and co-workers successfully prepared a solid solution of $\text{O}_3\text{-NaFe}_{1-y}\text{Ni}_y\text{O}_2$ ($0.5 \leq y \leq 0.7$).^[106] It's worthy to mention that some monoclinic impurity phases preferred to form when $0.1 \leq y \leq 0.4$, which is ascribed to the anisotropic low-spin Ni^{3+} that may induce large local lattice strain when replacing partial spherical Fe^{3+} . With the further increase of Ni^{3+} , this strain may be relieved by short-range ordering of Fe and Ni in MO_2 slab, thus allowing the formation of pure-phase solid solution.

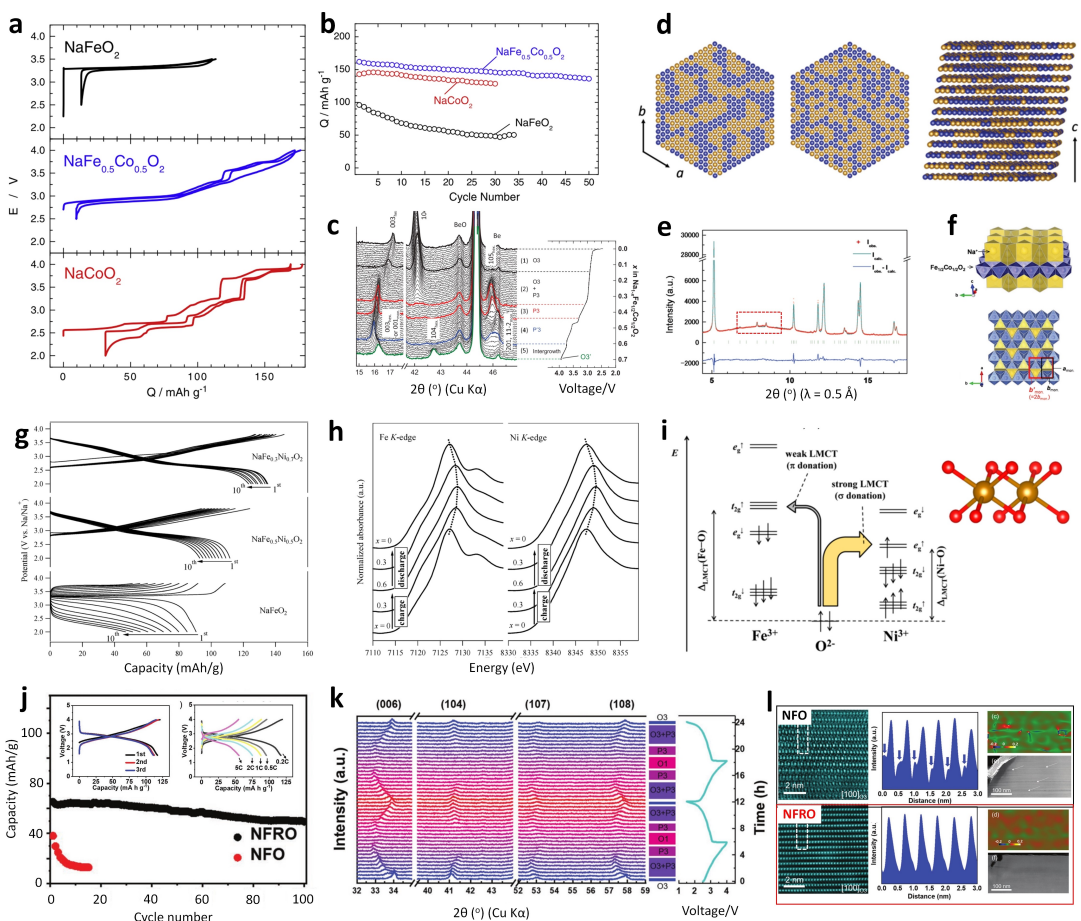


Figure 10. a) Charge/discharge curves of NaFeO_2 , $\text{NaFe}_{0.5}\text{Co}_{0.5}\text{O}_2$, and NaCoO_2 in Na cells at a rate of 12 mA g^{-1} , and b) corresponding cycling performances. a, b) Reproduced from Ref. [51] with permission. Copyright (2013) Elsevier. c) In-situ XRD patterns of $\text{NaFe}_{1-y}\text{Co}_y\text{O}_2$ electrode in the Na cell during galvanostatic charge at a rate of C/40. d) Snapshots of Fe (brown)/Co (blue) arrangement in $\text{NaFe}_{0.5}\text{Co}_{0.5}\text{O}_2$ compounds. e) Results of the Rietveld refinement on a powder X-ray diffraction pattern of $\text{Na}_{0.5}\text{Fe}_{0.5}\text{Co}_{0.5}\text{O}_2$, and f) schematic illustrations of the crystal structure. c–f) Reproduced from Ref. [107] with permission. Copyright (2016) Wiley-VCH. g) Charge/discharge curves of $\text{NaFe}_{1-y}\text{Ni}_y\text{O}_2$ compounds during the initial 10 cycles tested at 30 mA g^{-1} . h) Fe K-edge and Ni K-edge XANES spectra for $\text{Na}_{1-x}\text{Fe}_{0.3}\text{Ni}_x\text{O}_2$. i) Schematic Illustration of Ligand-to-Metal Charge Transfer (LMCT) in $\text{NaFe}_{1-y}\text{Ni}_y\text{O}_2$. g, i) Reproduced from Ref. [106] with permission. Copyright (2014) American Chemical Society. j) Cycle performances of the $\text{Na}/\text{Na}_2\text{FeRuO}_6$ and Na/NaFeO_2 cells at a rate of 2 C (insets: charge/discharge curves of $\text{Na}/\text{Na}_2\text{FeRuO}_6$ cell tested at varied current rates). k) In-situ XRD patterns of $\text{Na}_2\text{FeRuO}_6$ electrode for the initial two cycles. l) Comparison of atomic STEM-HAADF images and line-profile of selected area (pristine states), geometric phase analysis (GPA) patterns and particle crack images (charged to 4.0 V) for $\text{Na}_2\text{FeRuO}_6$ (bottom) and NaFeO_2 (top). j–l) Reproduced from Ref. [78] with permission. Copyright (2020) Wiley-VCH.

Among these materials, O3-NaFe_{0.3}Ni_{0.7}O₂ exhibits the best electrochemical performances, delivering a reversible capacity of 135 mAh g⁻¹ within 3.8–2.0 V in the first cycle. After 30 cycles, about 74% of the initial capacity remains (Figure 10g). In the fully charged state (3.8 V), the stoichiometry and nominal electronic structure is found to be Na_{0.4}Fe⁴⁺_{0.07}Fe³⁺_{0.23}Ni⁴⁺_{0.53}Ni³⁺_{0.27}O₂ according to the capacity and ⁵⁷Fe Mössbauer spectroscopy results. Thus, the enhanced structural stability compared with NaFeO₂ can be attributed to the less fraction of unstable Fe⁴⁺ together with the major contribution of Ni^{3+/4+} redox couple. XANES measurements further confirm the contribution of both Fe^{3+/4+} and Ni^{3+/4+} redox couple. One point should be noted is that a shift of the main peak of Fe K-edge spectra occurs at the initial stage of charging process. However, Fe⁴⁺ is not found until $x > 0.3$ in Na_{1-x}Fe_{0.3}Ni_{0.7}O₂ (Figure 10h). This contradiction is finally ascribed to the delocalized frontier electron/hole via ligand-to-metal charge transfer (LMCT) in Ni/Fe–O bands (Figure 10i). In other words, the oxidation of Ni³⁺ to Ni⁴⁺ decreases the 3d electron density of Fe, inducing large shift of Fe K-edge absorption but without changing the valence state. The enhanced charge delocalization efficiently suppresses local distortion of the Jahn-Teller Ni³⁺, which is also believed to be responsible for the improved cycle stability.

Although Co/Ni substitution exhibit great effectiveness in improving the electrochemical performance of O3-NaFeO₂, new research focused on Fe–Co or Fe–Ni based binary materials are rarely reported to date. One possible reason is that introducing a large fraction of Co/Ni is not in accord with the trend of developing low-cost cathodes for SIBs due to the limited source and ever-growing price of Co/Ni. More commonly, adding a small amount of Co and/or Ni into a ternary or multi-element system would be more acceptable in an overall consideration of performance and cost which will be discussed later in this article.

3.2.3. Other Fe-Based Binary Materials

Substitution of Ni with Ti is reported as an effective way to stabilize the structure of NaNiO₂ via suppressing multiple phase transition and smoothing charge/discharge profile.^[108] However, this strategy fails to work for NaFeO₂. In O3-type Na_xFe_xTi_{1-x}O₂ ($0.75 \leq x \leq 1.0$), the Fe^{3+/4+} redox couple is of poor reversibility accompanied with large polarization during charge/discharge process.^[109] Moreover, these materials suffer from dramatic capacity fading when Fe³⁺ oxidation occurs, which is ascribed to severe ion migration. Recently, Xu et al reported a Ru-doping strategy to suppress Fe-ion migration in NaFeO₂.^[78] In the obtained O3-type Na₄FeRuO₆ (NFRO), partial Na⁺ occupy at TM sites, while Na and [Na_{1/3}Fe_{1/3}Ru_{1/3}] slabs form alternate layers in the array of cubic close packed oxide-ions. Actually, this is a typical A₂MO₃ type layered material, of which the most famous prototype is Li₂MnO₃.^[110] Therefore, it seems more accurate to describe the obtained NFRO as a Fe-substituted Na₂RuO₃ or Fe/Na co-doped NaFeO₂. NFRO cathode delivers a reversible capacity of 120 mAh g⁻¹ at 0.2 C within 2–4 V, which

is much higher than that of NaFeO₂ (70 mAh g⁻¹). When cycled at 2 C, 80% of the initial capacity remains after 100 cycles, indicating a good reversibility of NFRO (Figure 10j). Such enhanced electrochemical performances are ascribed to the suppressed Fe migration and thus the inhibited irreversible O3-O'3-O'3 phase transition and particle cracks during cycling thanks to Ru-doping, as supported by in-situ XRD and ex-situ STEM-HAADF analysis results (Figure 10k, l). Although it seems debatable to attribute all these improvements to Ru-doping since those Na ions located at TM sites and the largely decreased Fe content may both have contributions, this work offers new strategy to develop cycle-stable Fe-based layered cathodes.

3.3. Fe-Based Ternary Oxides and Beyond

In comparison with pristine NaFeO₂, most binary materials with single-element doping have shown encouraging enhancements in both reversible capacity and cycling stability. However, their performances are far from satisfactory in regarding of practical utilizations, especially the performances of those materials with high Fe content. In this case, many efforts have been devoted to develop Fe-based or Fe-containing layered materials with ternary and even multi-element compositions, aiming to achieve better electrochemical behaviors through the synergistic effects. In these materials, Fe is employed as an important component to contribute moderate capacities at high-voltage region and to lower down the total material cost. Note that, considering the merits of high capacities and low costs, Fe–Mn based binary oxides have been majorly adopted as the footstones to develop ternary and multi-element layered cathodes. Functional cations such as Li, Ni, Cu, Al, and Ti et al. have been imported into Fe–Mn binary system to explore high-capacity and cycle-stable layered cathodes.

3.3.1. Na_x[Fe_yNi_zMn_{1-y-z}]O₂ ($0 < x \leq 1$, $0 < y < 1$, $0 < z < 1-y$)

To overcome the capacity fading of P2-type Na_{2/3}Fe_{1/2}Mn_{1/2}O₂, Talaie et al. propose to substitute Fe³⁺ with Ni²⁺/Mn⁴⁺ to mitigate Fe³⁺ migration at high voltage.^[61,111] Note that, transition metal migration from TM octahedral sites to neighbor tetrahedral sites in Na layer, which is proposed as the driving force of short-range ordering with O2-type stacking, is successfully probed by X-ray pair distribution function (PDF) analysis for the first time in this work (Figure 11a). In-situ XRD results further demonstrate that such P–O phase transition has been delayed after Ni-substitution (Figure 11b). However, the obtained Na_{0.67}Ni_{0.15}Fe_{0.2}Mn_{0.65}O₂ still suffers from fast capacity fading when cycled in a wide voltage range of 4.3–1.5 V since P2–“Z” and P2–P’2 phase transition remain. Better cycling stabilities can be achieved by narrowing the voltage window to 4.1–2 V, although at the expense of capacity. Encouragingly, the elevated discharge voltage contributed by Ni^{2+/4+} redox couple compensate such capacity loss, resulting in an enhanced energy density (Figure 11c). Similarly, Hasa et al.

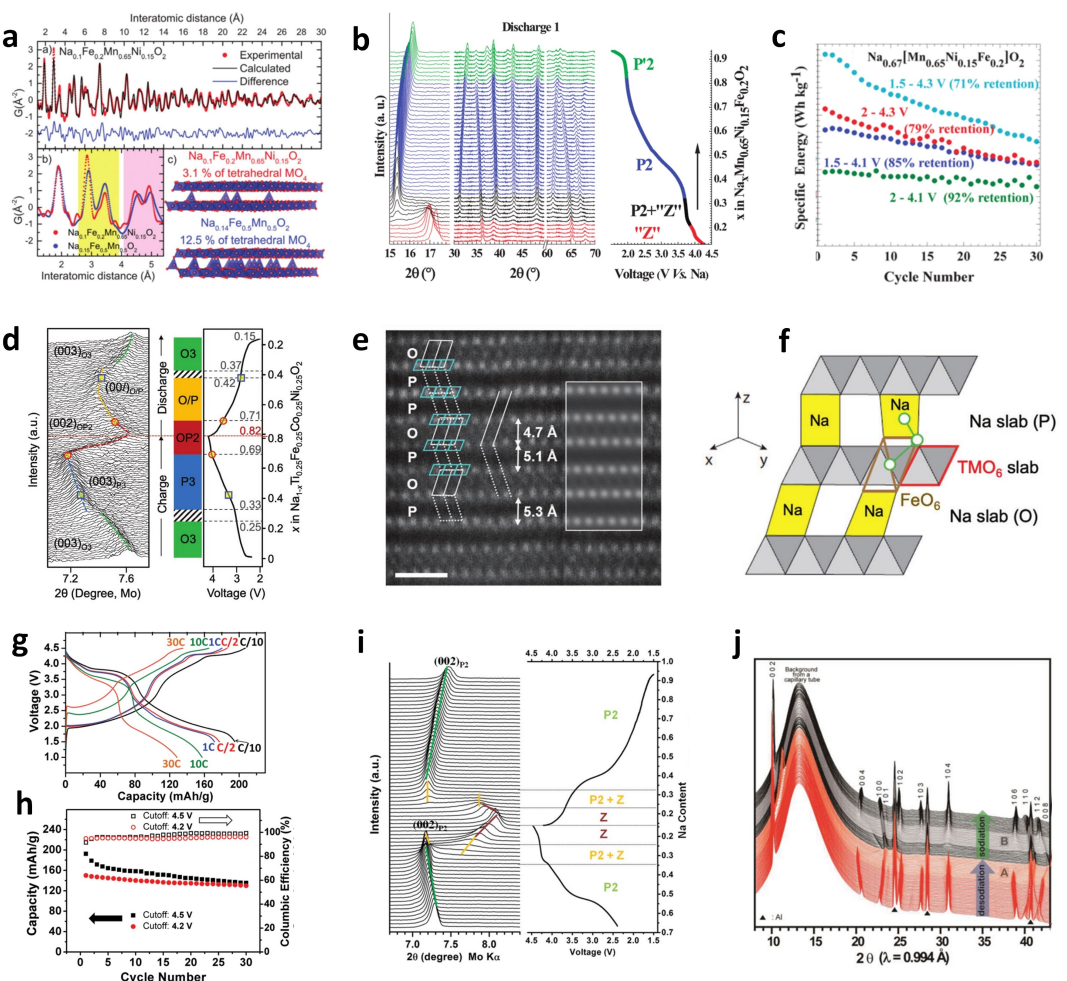


Figure 11. a) Fit of the PDF curves of chemically oxidized Z-Na_{0.1}Fe_{0.2}Mn_{0.65}Ni_{0.15}O₂, comparison of the short range experimental PDF of Z-Na_{0.1}Fe_{0.2}Mn_{0.65}Ni_{0.15}O₂ and Z-Na_{0.14}Fe_{0.5}Mn_{0.5}O₂, and corresponding illustration of the two structures. b) In-situ XRD data recorded during galvanostatic cycling of Na_{0.67}[Mn_{0.65}Ni_{0.15}Fe_{0.2}]O₂ at a rate of C/20. c) Specific energy of Na_{0.67}[Mn_{0.65}Ni_{0.15}Fe_{0.2}]O₂ (right) as a function of cycle number. a–c) Reproduced from Ref. [61] with permission. Copyright (2016) Royal Society of Chemistry. d) In situ XRD evolution for (001) peak of O3-NaTi_{0.25}Fe_{0.25}Co_{0.25}Ni_{0.25}O₂ as a function of the Na content. e) HAADF-STEM images of Na_{0.22}Ti_{0.25}Fe_{0.25}Co_{0.25}Ni_{0.25}O₂ (4.2 V). f) Schematic of an Fe⁴⁺O₆ octahedron in OP2 stacking, which interacts with non-Jahn-Teller-activated TMO₆ octahedron (red outline) and prismatic/octahedral Na. d–f) Reproduced from Ref. [122] with permission. Copyright (2020) Wiley-VCH. g) Charge/discharge curves at varied current rates, h) capacity retention within different voltage ranges, and i) in-situ XRD data collected during initial cycle for Na_{2/3}Co_{1/4}Fe_{1/4}Mn_{1/2}O₂. g–i) Reproduced from Ref. [123] with permission. Copyright (2015) Wiley-VCH. j) In-situ SXRD patterns of Na_{0.7}Co_{0.2}Fe_{0.4}Mn_{0.4}O₂ electrode and corresponding charge/discharge curve. Reproduced from Ref. [124] with permission. Copyright (2015) Wiley-VCH.

have reported a P2 type Na_{0.5}Ni_{0.23}Fe_{0.13}Mn_{0.63}O₂ cathode, demonstrating a maximum capacity over 200 mAhg⁻¹. Fast capacity deterioration occurs at the initial charge/discharge stage, while it becomes stable in following cycles.^[112] Such enhanced electrochemical performances compared to Na_{0.67}Ni_{0.15}Fe_{0.2}Mn_{0.65}O₂ could be originated from the increased content of Ni along with the decreased Fe.

O3-type NaNi_{1/3}Fe_{1/3}Mn_{1/3}O₂ is another typical Ni–Fe–Mn based ternary cathode material. In the sodium half-cell, it delivers a reversible capacity over 130 mAhg⁻¹ within 4.0–2.0 V, accompanied with a reversible O3-P3 phase transition process.^[52,113] The moderate working voltage (over 3.0 V), acceptable cycling stability (more than 80% capacity retention after 100 cycles), together with the sufficient Na content and low cost have made it a promising cathode for full-cell applications. To further improve its cycling stability, strategies such as Fluorine-doping and calcium-doping are proposed,

both showing positive effects.^[114,115] However, more in-depth investigations are still needed to fully understand the capacity fading of NaNi_{1/3}Fe_{1/3}Mn_{1/3}O₂, so as to figure out targeted approaches for further improvements.^[116] Notably, supported by synchrotron-based analysis, Jeong and co-workers claimed that O3-P3 phase transition only majorly under charging voltage of 4.0 V, while Ni²⁺/Ni⁴⁺ redox couple contributes most of capacity in this region.^[117] When charged above 4.0 V, Fe³⁺/Fe⁴⁺ reactions become dominant, leading to increased distortion of local structure for Fe. As charging process goes on, P3 phase is finally transformed into OP2 structure with collapsed d-spacing, possibly due to the migration of Fe into Na sites. Very recently, by using HAADF-STEM, such OP2 structure was directly observed in a ternary O3-type NaTi_{0.25}Fe_{0.25}Co_{0.25}Ni_{0.25}O₂ (NaTFCN) after charging to 4.2 V (Na_{0.22}TFCN) (Figure 11d, e). Meanwhile, a novel viewpoint was proposed that such unique structure may originated from the

atomic interactions involving Jahn-Teller active Fe^{4+} and distortion tolerant Ti^{4+} that stabilize the local Na environment (Figure 11f). This could offer new insight to understanding the high-voltage phase of Fe-based layered oxides. As a short conclusion, limiting the working voltage window, e.g., charging below 4.0 V, seems to be quite important for Fe-based layered cathodes to achieve better cycling stabilities. For example, although containing higher Fe contents compared with $\text{NaNi}_{1/3}\text{Fe}_{1/3}\text{Mn}_{1/3}\text{O}_2$, O3-type $\text{NaFe}_{0.4}\text{Ni}_{0.3}\text{Mn}_{0.3}\text{O}_2$ and $\text{NaNi}_{0.25}\text{Fe}_{0.5}\text{Mn}_{0.25}\text{O}_2$ exhibit even higher reversible capacities and better rate/cycling performances within the limited voltage range of 2–3.8 V and 2.1–3.9 V, respectively.^[118,119]

Qi and co-workers proposed to design Ni–Fe–Mn ternary oxides with O3/P2 hybrid structures. As a successful prototype, the obtained $\text{Na}_{0.78}\text{Ni}_{0.2}\text{Fe}_{0.38}\text{Mn}_{0.42}\text{O}_2$, consisting of 37.14% of P2 phase and 62.86% of O3 phase, delivers a capacity of 86 mAh g^{-1} within 4–2.5 V, accompanied with good rate capability and cycling performances. Note that, such hybrid materials have attracted increased attentions in recent years, which may offer new insights to design advanced cathodes for SIBs.^[120] In addition, air-instability is another issue of Ni–Fe–Mn based ternary oxides. Coating with stable surface layers, e.g. MnO_2 and ZrO_2 , are proposed as a potential way to solve this problem.^[116,121]

3.3.2. $\text{Na}_x[\text{Fe}_y\text{Co}_z\text{Mn}_{1-y-z}]\text{O}_2$ ($0 < x \leq 1$, $0 < y < 1$, $0 < z < 1-y$)

By importing Mn into Fe–Co based binary oxides, a ternary P2-type $\text{Na}_{2/3}\text{Mn}_{1/3}\text{Fe}_{1/3}\text{Co}_{1/3}\text{O}_2$ material was obtained and utilized as cathode for SIBs, showing a maximum discharge capacity of about 173 mAh g^{-1} within 4.3–1.5 V and an energy density of about 520 Wh kg^{-1} .^[125] However, this material undergoes fast capacity fading unless the charging cut-off voltage is below 4.1 V. Further increasing the proportion of Mn, Liu et al. reported a P2-type $\text{Na}_{2/3}\text{Mn}_{1/2}\text{Fe}_{1/4}\text{Co}_{1/4}\text{O}_2$, which demonstrates an enhanced cycling stability with the voltage range of 1.5–4.2 V.^[123] When charged to 4.5 V, fast capacity fading would occur. Moreover, this material exhibits outstanding rate performances, demonstrating a capacity of 130 mAh g^{-1} at 30 C rate (7.74 A g^{-1}) (Figure 11g, h). In-situ XRD analysis further points out that this material majorly experiences a single P2-phase evolution except for a P2-Z phase transition process emerging at high-voltage region (Figure 11i). Notably, the larger single-phase zone (without P'2 phase appearing in high sodiation states) than many other reported layered cathode materials is attributed to the reduction of Co^{3+} to Co^{2+} instead of fully reduction of Mn^{4+} to Mn^{3+} during discharging process. In the same period of time, a series of Co-substituted P2-type $\text{Na}_{0.7}(\text{Fe}_{0.5}\text{Mn}_{0.5})_{1-x}\text{Co}_x\text{O}_2$ materials were reported, exhibiting high initial capacity within 4.5–1.5 V. Accompanied with reversible P2-O2 phase transition at above 4.1 V, all of them undergo fast capacity fading in following cycles. Their *in-situ* XRD also confirmed that no P'2 phase formed at the end of discharge (1.8 V) (Figure 11j). Therefore, it seems that P2-P'2 phase transition which generally occurs in P2-type Fe–Mn based oxides can be efficiently suppressed by introducing Co.

However, the reduction of Co^{3+} to Co^{2+} during deep discharging process was not detected in the later work according to ex-situ XAS at Co K-edge. It may call for further investigation to clarify the suppressed phase transition.

3.3.3. $\text{Na}_x[\text{Fe}_y\text{Cu}_z\text{Mn}_{1-y-z}]\text{O}_2$ ($0 < x \leq 1$, $0 < y < 1$, $0 < z < 1-y$)

$\text{Cu}^{2+/3+}$ redox couple was discovered to be electrochemically active in sodium layered cathodes in 2015, which then set off a wave of investigation on Cu-based materials.^[50] Coupling Cu with Fe–Mn based layered oxides is another milestone that offers a new choice of cathode materials to build cost-effective SIBs.^[126–132] Note that, Cu–Fe–Mn ternary oxides, such as P2-type $\text{Na}_{7/9}\text{Cu}_{2/9}\text{Fe}_{1/9}\text{Mn}_{2/3}\text{O}_2$ and O3-type $\text{Na}_{0.9}\text{Cu}_{0.22}\text{Fe}_{0.3}\text{Mn}_{0.48}\text{O}_2$, exhibit outstanding stabilities even when soaked in water, which is mainly attributed to the incorporation of Cu and the resulted higher average sodium-storage voltages.^[53,127] By integrating $\text{Cu}^{2+}/\text{Cu}^{3+}$ and $\text{Fe}^{3+}/\text{Fe}^{4+}$ redox couples, P2-type $\text{Na}_{7/9}\text{Cu}_{2/9}\text{Fe}_{1/9}\text{Mn}_{2/3}\text{O}_2$ delivers a reversible capacity of 89 mAh g^{-1} (0.1 C within 4.2–2.5 V) with an average discharge voltage of 3.6 V, while O3-type $\text{Na}_{0.9}\text{Cu}_{0.22}\text{Fe}_{0.3}\text{Mn}_{0.48}\text{O}_2$ yields over 100 mAh g^{-1} (0.1 C within 4.05–2.5 V) with an average voltage of 3.2 V (Figure 12a, b). Such high working voltages endow both cathodes with 300 Wh kg^{-1} class energy densities, in spite of the moderate capacities. Good structural reversibility of both materials during cycling are also observed, notably, this may be partially resulted from the modest Na^+ extraction/insertion with relatively small structure changes.

In recent years, growing interests have been focused on disclose the electrochemical behaviors of Cu–Fe–Mn ternary oxides in extended voltage ranges. Supported by *in-situ* XRD/XANES and ex-situ PDF analysis of P2-type $\text{Na}_x[\text{Mn}_{0.66}\text{Fe}_{0.2}\text{Cu}_{0.14}]\text{O}_2$, Talaie and co-workers observed P2–“Z” phase transition at high-voltage region above 4.1 V which is originated from the migration of transition metal ions, leading to large polarizations, capacity fading, and voltage deterioration.^[126] Moreover, the capacities obtained at high-voltage region of 4.1–4.3 V can be explained neither by the charge compensation from cationic redox due to the unchanged XANES spectra of transition-metal ions nor by the electrolyte decomposition or oxygen release in view of the reversible structural evolution of bulk material. Instead, all the results well indicate the reversible reaction of anion redox, while more direct evidence are still needed to prove this point. Similarly, Xu et al. preferred to ascribe the capacity of $\text{Na}_{0.7}[\text{Cu}_{0.2}\text{Fe}_{0.2}\text{Mn}_{0.6}]\text{O}_2$ at high-voltage region to the ligand charge transfer (MLCT) contributed by both Cu–O and Fe–O redox centers.^[128] Meanwhile, voltage decay in Fe-based layered oxides is also attributed to Fe migration, which can be efficiently mitigated by Cu/Fe exchange. One of the possible reasons given by DFT simulation is that the neighboring Cu^{2+} with large electronegativity can shorten the Fe–O bond length, thus increasing the energy barrier of Fe migration.^[133] Regarding the deep-discharge region, the participation of $\text{Mn}^{3+}/\text{Mn}^{4+}$ redox couple show significant influences upon the electrochemical behaviors of Cu–Fe–Mn ternary cathodes. For those materials with low

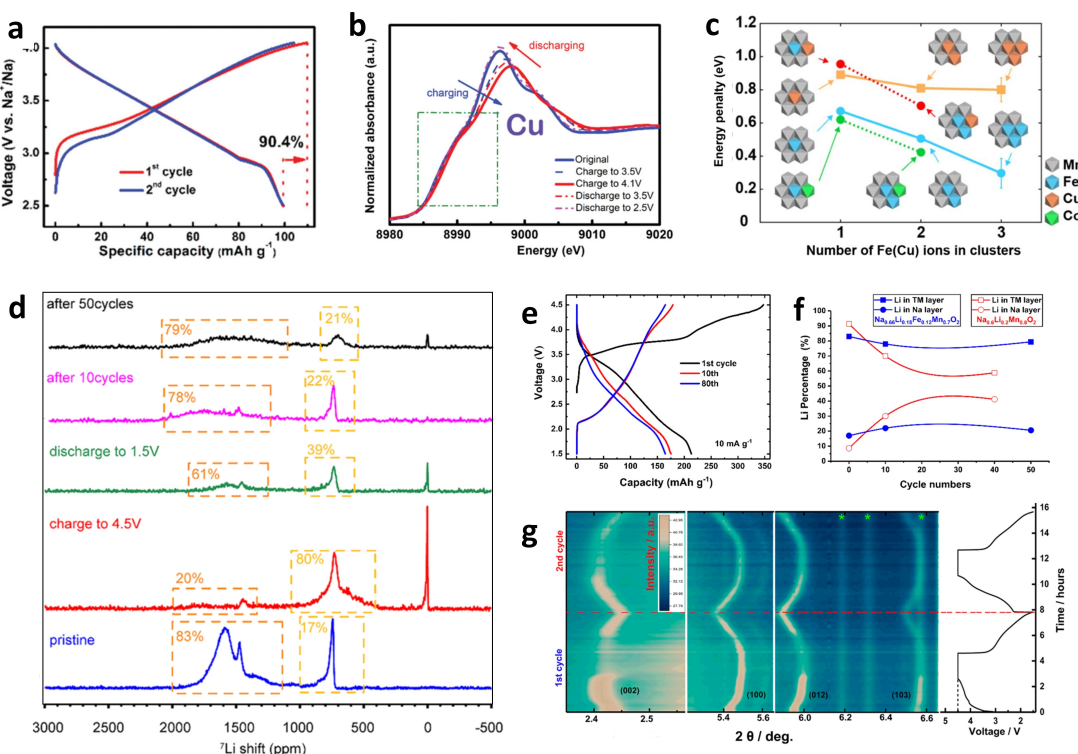


Figure 12. a) Charge/discharge curves of O3-type $\text{Na}_{0.9}\text{Cu}_{0.22}\text{Fe}_{0.3}\text{Mn}_{0.48}\text{O}_2$ electrode for the initial two cycles, and b) corresponding Cu K-edge XANES collected at different state of charge. a, b) Reproduced from Ref. [53] with permission. Copyright (2015) Wiley-VCH. c) Energy penalties for the TM migration in O2 phase depending on the composition Of TM ions. Reproduced from Ref. [133] with permission. Copyright 2021, Wiley-VCH. d) ^7Li NMR spectra of P2- $\text{Na}_{0.66}\text{Li}_{0.18}\text{Fe}_{0.12}\text{Mn}_{0.7}\text{O}_2$ electrodes collected at different state of charge. e) Selected charge/discharge curves of $\text{Na}_{0.66}\text{Li}_{0.18}\text{Fe}_{0.12}\text{Mn}_{0.7}\text{O}_2$ electrode tested at 10 mA g^{-1} . f) Variation of fractions of Li in TM layers and Li in Na layers for $\text{Na}_{0.6}\text{Li}_{0.2}\text{Mn}_{0.8}\text{O}_2$ and $\text{Na}_{0.66}\text{Li}_{0.18}\text{Fe}_{0.12}\text{Mn}_{0.7}\text{O}_2$. g) In-situ XRD patterns of $\text{Na}_{0.66}\text{Li}_{0.18}\text{Fe}_{0.12}\text{Mn}_{0.7}\text{O}_2$ collected during initial two cycles. d–g) Reproduced from Ref. [134] with permission. Copyright (2019) American Chemical Society.

pristine valences of Mn, discharge capacities can be largely increased when lowering down discharging cut-off voltage owing to the contribution of $\text{Mn}^{3+}/\text{Mn}^{4+}$ redox couple, followed by degraded capacity retentions due to the severe Jahn-Teller distortions induced by Mn^{3+} .^[131,132] It should be noticed that, although Cu-substitution could markedly modify the structural and electrochemical properties of Fe–Mn based oxides, the proportion of Cu can hardly been further increased in this system due to the limitation of solid solubility and complicated influences of elemental valences.^[131,132] In other words, elaborate design of composition is required to develop high-performance Cu–Fe–Mn ternary cathode materials.

3.3.4. Other Ternary Oxides

Other elements such as Mg, Al, and Nb have also been explored as dopants to overcome the capacity fading issues of Fe–Mn binary cathodes.^[135–139] Al-doping could slightly increase the electrical conductivity and Na-ion diffusivity of O3-type $\text{NaFe}_{0.5}\text{Mn}_{0.5}\text{O}_2$. However, negligible improvements on the kinetics and stabilities of the electrochemical reaction were observed.^[135] By contrast, Nb-doping in O3-type $\text{NaFe}_{0.55}\text{Mn}_{0.45}\text{O}_2$ obviously enhances both the rate capabilities and cycling stabilities of the parent material owing to larger lattice spacing, better reversibility of O3-P3 phase transition,

and higher material conductivity.^[137] For P2-type $\text{Na}_{2/3}\text{Fe}_{1/2}\text{Mn}_{1/2}\text{O}_2$, it is reported that Al-substitution for Mn or Fe could promote Na^+ diffusion and strengthen structural stability by manipulating lattice spacing and TM–O/O–O bonding, resulting in improved rate and cycling performances, particularly in the case of Al substituting for Fe.^[136] Zhou et al. obtained a P2/O3 bi-phase $\text{Na}_{0.67}\text{Fe}_{0.425}\text{Mn}_{0.425}\text{Mg}_{0.15}\text{O}_2$ by using Mg substitution, demonstrating enhanced capacity retention in comparison with $\text{Na}_{2/3}\text{Fe}_{1/2}\text{Mn}_{1/2}\text{O}_2$. Note that, according to recent reports about Mg-substituted layered materials, Mg^{2+} can be induced into both Na sites and TM sites.^[140,141] Consequently, clarifying the actual occupying position of Mg^{2+} is quite important to understand the electrochemical behaviors of these modified materials.

As for some reported Fe-containing ternary oxides, Fe element is actually employed as dopant to tailor the phase structure and electrochemical properties certain parent materials, e.g., Mn-rich oxides. Yang and co-workers prepared a P2-type $\text{Na}_{0.66}\text{Li}_{0.18}\text{Fe}_{0.12}\text{Mn}_{0.7}\text{O}_2$ cathode material by co-doping Li and Fe into the TM layers of $\text{Na}_{0.67}\text{MnO}_2$.^[134] Compared with the pristine Mn-based oxide, Fe doping brings higher discharge voltage and thus the energy density. More impressively, it is proved by NMR that Li^+ could hop reversibly between TM layer and Na layer during Na^+ extraction/insertion process (Figure 12d). Such unique behaviors occurring at a wide voltage range of 4.5–1.5 V well offset the interslab instability induced

by deep Na^+ extraction, thus significantly suppressing P2-O2 phase transition and enabling a highly reversible capacity of 214 mAh g^{-1} (Figure 12e, g). Moreover, Fe-doing likely help to mitigate the Li loss from TM layer upon cycling for unclear reasons, which is considered as another factor for the excellent capacity retention (Figure 12f). Recently, Fe substitution were successfully utilized to stabilize the host structure of P2 and P'2 type Na_xMnO_2 .^[142–145] Hwang and co-workers proposed a P2-type $\text{Na}_{0.55}[\text{Ni}_{0.1}\text{Fe}_{0.1}\text{Mn}_{0.8}]\text{O}_2$ material, which exhibits an ultra-high capacity of 221.5 mAh g^{-1} within 4.3–1.5 V and an average discharge voltage of 2.9 V. However, such high capacity cannot be well maintained during cycling owing to the P2-OP4 phase transition observed within 4.1–4.3 V. Good cycling stabilities were further achieved when limiting the cut-off voltage within 3.9–1.5 V. Note that, P'2 type Mn-based materials have attracted increasing interests in the recent years for smoother voltage profile and higher energy density compared with their P2-type counterparts.^[93] Current researches on these P'2 type Mn-based material are mainly focused on understanding the unique electrochemical behaviors and improving their cycling stabilities.^[146] Choi and co-workers reported that Fe/Mn replacement could suppress Jahn-Teller effects of Mn^{3+} in P'2- $\text{Na}_{2/3}\text{MnO}_2$, thus alleviating capacity deterioration during cycling.^[145] Moreover, Fe/Ti co-substituted P'2- $\text{Na}_{0.67}[(\text{Mn}_{0.78}\text{Fe}_{0.22})_{0.9}\text{Ti}_{0.1}]\text{O}_2$ demonstrates a single phase reaction within 4.3–1.5 V, delivering a highly reversible capacity of 180 mAh g^{-1} . Such excellent structural flexibility is attributed to the sequence of $\text{Mn}-\text{O}-\text{Ti}-\text{O}-\text{Fe}$ in transition metal layer.^[143] Similarly, it is claimed that, the O–Ni–O–Mn–O–Fe–O bond in transition-metal layers remarkably suppress the structural distortion of P'2- $\text{Na}_{0.67}[\text{Ni}_{0.1}\text{Fe}_{0.1}\text{Mn}_{0.8}]\text{O}_2$, resulting in high capacities over 220 mAh g^{-1} and good cycling stabilities even if the P'2-OP4 phase transition occurring in high-voltage region.^[144] In these Mn-rich materials, Fe element plays important roles in contributing capacities at high-voltage region and suppressing the elongation of the Mn–O bond.

In addition, ternary oxides without Mn element have also been investigated. In comparison with $\text{NaNi}_{1/3}\text{Fe}_{1/3}\text{Mn}_{1/3}\text{O}_2$, O3-type $\text{NaNi}_{1/3}\text{Fe}_{1/3}\text{Co}_{1/3}\text{O}_2$ demonstrates a higher reversible capacity of 165 mAh g^{-1} within 4.2–2.0 V contributed by $\text{Ni}^{3+}/\text{Ni}^{4+}$, $\text{Fe}^{3+}/\text{Fe}^{4+}$, and $\text{Co}^{3+}/\text{Co}^{4+}$. Moreover, 80 mAh g^{-1} can be maintained at an ultra-high rate of 30 C (7.12 A g^{-1}), indicating outstanding rate capabilities, which are commonly seen for Co-based cathode materials. However, fast capacity fading and the high cost of Co make it hard for practical utilizations. Wang^[147] reported an O3-type $\text{NaFe}_{1/3}\text{Ni}_{1/3}\text{Ti}_{1/3}\text{O}_2$ cathode, which displays a reversible capacity of 117 mAh g^{-1} within 4–1.5 V followed by good cycling stability. Note that, this capacity is majorly contributed by redox reactions of Ni, while Fe only yields small capacity via the redox couple of $\text{Fe}^{2+}/\text{Fe}^{3+}$. Such a suppressed activity of Fe is strange and may needs further investigations.

3.3.5. Multi-Element Oxides

Designing layered cathodes with multi-element compositions offers the opportunity to integrate distinct merits of different

metal ions. In order to combine the excellent cycling stability of $\text{O3-NaFe}_{1/2}\text{Co}_{1/2}\text{O}_2$ and high capacity of $\text{O3-NaNi}_{1/2}\text{Mn}_{1/2}\text{O}_2$, Li and co-workers proposed an O3-type compound with quaternary composition of $\text{NaMn}_{1/4}\text{Fe}_{1/4}\text{Co}_{1/4}\text{Ni}_{1/4}\text{O}_2$.^[148] With the participation of all the transition metal ions in redox reactions, this material shows a high capacity of 180 mAh g^{-1} with an average discharge voltage of 3.21 V, generating a specific energy over 578 Wh kg^{-1} (Figure 13a). When cycled within 4.3–1.5 V, it exhibits much slower capacity fading than $\text{NaFe}_{1/2}\text{Co}_{1/2}\text{O}_2$ and $\text{NaNi}_{1/2}\text{Mn}_{1/2}\text{O}_2$, indicating the merits of such quaternary materials. Oh et al. prepared an O3-type $\text{Na}[\text{Li}_{0.05}(\text{Ni}_{0.25}\text{Fe}_{0.25}\text{Mn}_{0.5})_{0.95}]\text{O}_2$ by doping Li into the transition layer in $\text{NaNi}_{0.25}\text{Fe}_{0.25}\text{Mn}_{0.5}\text{O}_2$.^[149] The introduction of Li greatly stabilizes the host structure due to the strong Li–O bonds, resulting in the delay of O3-P'3 phase transition. Consequently, a high capacity of 180.1 mAh g^{-1} as well as good rate and cycling performances are obtained (Figure 13b, c). Similarly, You et al. reported a Li-doped O3-type $\text{Na}_{0.85}\text{Li}_{0.1}\text{Ni}_{0.175}\text{Mn}_{0.525}\text{Fe}_{0.2}\text{O}_2$, delivering 157 mAh g^{-1} within 4.5–2.0 V and a high specific energy of 529 Wh kg^{-1} .^[150] Thanks to the improved reversibility of O3-P3 phase transition and inhibited loss of active transition metal ions at high voltage, good rate capabilities and high capacity retentions are also achieved (Figure 13d–f). Mu et al. substituted partial Ni with Cu in $\text{NaNi}_{1/3}\text{Fe}_{1/3}\text{Mn}_{1/3}\text{O}_2$, also obtaining a cathode material with enhanced kinetics and cycling stability.^[152] It is worth to mention that, recently, high entropy layered oxide cathodes as a new concept of multi-element materials are proposed. The unique electrochemical behaviors of such kind of materials may provide new insights to design advanced layered cathodes for SIBs (Figure 13g, h).^[151]

4. Issues, Challenges, and Perspectives

The discovery of the electrochemically activity of $\text{Fe}^{3+}/\text{Fe}^{4+}$ redox couple in sodium layered materials has offered new chances to design high capacity/voltage and low-cost cathodes for SIBs. However, issues and challenges still exist in developing Fe-based layered cathode materials for practical utilizations. As following, these issues and challenges are summarized and discussed. Accordingly, some perspectives are also proposed.

4.1. Iron Migration

For Fe-based layered materials, the migration of Fe ions between transition metal layer and sodium layer occurring in high-voltage region (deep desodiation states) has been widely reported. The well recognized mechanism is that Fe tends to migrate from pristine octahedral site in the TM layer into its face-shared tetrahedral site in the Na layer (Figure 6a), where is energy favorable for the occupation of trivalent Fe, especially when a large amount of Na^+ vacancies have been created upon sodium extraction.^[35,61,64] Although such migrations are likely reversible during charge/discharge cycling, they would cause large polarizations, slow Na^+ diffusion, huge volume

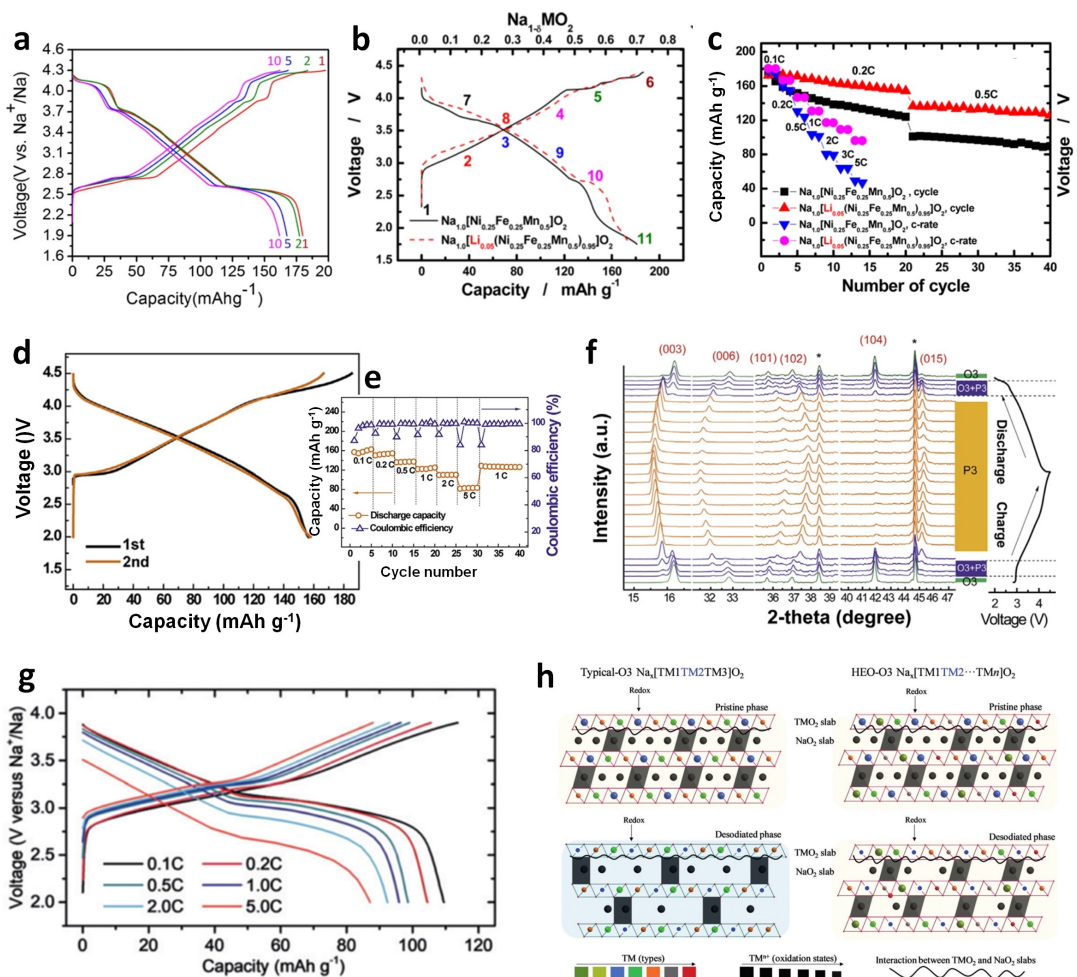


Figure 13. a) Selected charge/discharge curves of O_3 -type $\text{NaMn}_{1/4}\text{Fe}_{1/4}\text{Co}_{1/4}\text{Ni}_{1/4}\text{O}_2$ electrode. Reproduced from Ref. [148] with permission. Copyright (2014) Elsevier. b, c) Comparison of b) initial charge curve and c) rate and cycling performances for O_3 -type $\text{Na}[\text{Li}_{0.05}(\text{Ni}_{0.25}\text{Fe}_{0.25}\text{Mn}_{0.5})_{0.95}\text{O}_2]$ and $\text{NaNi}_{0.25}\text{Fe}_{0.25}\text{Mn}_{0.5}\text{O}_2$ electrode. Reproduced from Ref. [149] with permission. Copyright (2014) American Chemical Society. d) Initial charge/discharge curves, e) rate performances, and f) in-situ XRD patterns of O_3 -type $\text{Na}_{0.85}\text{Li}_{0.1}\text{Ni}_{0.175}\text{Mn}_{0.525}\text{Fe}_{0.2}\text{O}_2$ electrode. d-f) Reproduced from Ref. [150] with permission. Copyright 2018, Elsevier. g) Charge/discharge curves of high-entropy $\text{NaNi}_{0.12}\text{Cu}_{0.12}\text{Mg}_{0.12}\text{Fe}_{0.15}\text{Co}_{0.15}\text{Mn}_{0.1}\text{Ti}_{0.1}\text{Sn}_{0.1}\text{Sb}_{0.04}\text{O}_2$ electrode at varied current rates. h) Possible mechanism of high-entropy composition in facilitating layered O_3 -type structure. Reproduced from Ref. [151] with permission. Copyright (2020) Wiley-VCH.

changes together with severe internal strain and even particle cracks, leading to capacity/voltage deteriorations.^[61,78,128] Substituting Fe with other cations is the most common way to overcome or mitigate this issue. However, significant mitigation of Fe migration has merely been noticed in those materials with low content of Fe. For those materials containing high content of Fe, limited charging cut-off voltages, which means constrained oxidation of Fe^{3+} , are needed to avoid Fe migrations. In other words, the migration of Fe largely depends on the concentration of Fe^{4+} . Based on DFT computation, Li et al. proposed that the formation of Fe cluster could greatly lower down the energy penalty for Fe migration in high-voltage O-type phase (O_2 and O_3 -like stacking) since the Jahn-Teller distortion of a neighboring Fe^{4+}O_6 octahedron can accommodate the shrink of the tetrahedron with a migrating Fe. Consequently, it indicates an optimal Fe composition of around 33% (in TM layer), agreeing well with reported experimental results.^[74] It is also suggested to introduce TM ions with large electronegative, such as Cu and Ru, as the

neighbor of Fe to stabilize Fe by shortening Fe–O bond length and increase the energy barrier of Fe migration.^[78,133] In this case, carefully designing the composition in TM layer can be one of the potential approaches to develop Fe-rich layered cathodes. Meanwhile, there are also some new viewpoints claiming that a small amount of Fe pinning in sodium layer may help to stabilize the host structure through the so-called “pillar effects”.^[153] Hence, more in-depth investigations are still demanded to further understand the migration of Fe and to fairly estimate its influence.

4.2. Phase Transition

As known, in contrast to lithium layered oxides, sodium layered oxides experience more complicated phase transitions during charge-discharge process because of larger volume change of unit cells induced by Na^+ extraction/insertion. These multiple phase transition processes are normally considered to be

unfavorable due to the accompanied issues such as stepwise voltage profile, structural defects, great internal stress, and sluggish ion diffusion et al.^[78,107,148] As for P2-type Fe-based layered materials, P2-OP4 (or P2-Z) and P2-P'2 phase transitions occur in deep desodiation and deep sodiation stage, respectively. Specifically, P2-OP4/Z phase transition is mainly ascribed to slab gliding derived from weakened interactions between TMO_2 layers and transition metal migration, and the formation of P'2 phase is induced by Jahn-Teller distortion of MnO_6 octahedrons.^[49,61,89,126] In regard to O3-type Fe-based materials, phase transition behaviors are related to the concentration of Fe in host structures. For NaFeO_2 , irreversible transition from O3 phase to O'3 and O''3 phase occurs along with Na^+ extraction due to the migration of Fe, resulting in drastic capacity loss within following cycles.^[70,71] For those materials with various dopants and relative lower content of Fe, reversible phase transitions such as O3-P3 and O3-P3-O'3 are generally observed.^[103,107] Note that, O3-P3 phase transition may be beneficial to facilitate Na^+ diffusion owing to the expanded space of sodium layer and suppressed Fe migration.^[113,117,147] However, transformation from P3 phase to O-type distorted structure such as O'3 and O1 phase emerging during further Na^+ extraction would degrade the Na^+ diffusion again due to the compressed interlayer distance, deteriorating rate and/or cycling performances.^[21,53,78] The key point to suppress the phase transitions at high-voltage region is to offset the interlayer instability generated by Na^+ extraction. In this case, strategies such as employing reversible migration of Li^+ and designing Na-site doped materials are of good choices since Li^+ or other doping ions located at Na sites (e.g., Mg^{2+} , K^+) could well bond adjacent TMO_2 slabs during Na^+ extraction via so-called “pinning” or “pillar effects”.^[134,140,141,154]

4.3. Oxygen Evolution and Side Reactions

Capacity fading originated from irreversible oxygen evolution and/or surface side reactions (e.g., electrolyte decomposition) is the common issue for layered cathode materials. In the case of Fe-based layered oxides, the participation of oxygen redox was once ignored in consideration of the less hybridization between trivalent iron and oxygen in sodium system (in comparison with Li system), which makes $\text{Fe}^{3+}/\text{Fe}^{4+}$ more favorable during charging process. However, it should be noted that tetravalent iron shows strong hybridization with the oxygen 2p orbital, as evidenced by the observed charge transfer from oxygen to iron in SrFeO_3 .^[155] Hence, the possibility of such a charge transfer process can hardly be negligible for Fe-based layered cathodes involving $\text{Fe}^{3+}/\text{Fe}^{4+}$ redox. To date, only a few papers have paid attention to the oxygen evolution in Fe-based layered cathodes, declaring the participation of oxygen redox triggered by Fe migration. More systematic study is still needed to gain a comprehensive understanding of the charge compensation and capacity deterioration for Fe-based layered oxides, especially for those materials with suppressed Fe migration. In addition, the side reaction between tetravalent iron and electrolyte at the surface area of particle also deserves

more attention since the electrode-electrolyte interface is quite crucial to the kinetics and cycling stability of electrode materials.

4.4. Air Stability

Air-stability is another common issue for layered cathode materials, including Fe-based oxides. Most of the reported Fe-based layered oxides suffer from structure deterioration when exposed in moist air due to the loss of Na from host structure accompanied with the reaction with CO_2 and H_2O .^[18,156] A recent work further clarify that the air-stabilities of P2-type layered oxides are correlated to the redox potential in the first cycles, which corresponds to the requested energy for chemical Na^+ extraction.^[157] For those layered materials relying on low-voltage redox couples such as $\text{V}^{3+}/\text{V}^{4+}$, $\text{Fe}^{3+}/\text{Fe}^{4+}$, and $\text{Mn}^{3+}/\text{Mn}^{4+}$, the loss Na^+ from the bulk to surface spontaneously occurs during air exposure. Meanwhile Na^+/H^+ exchange simultaneously happens for charge compensations, forming $\text{NaCO}_3/\text{NaHCO}_3$ layer at the surface of particles and leading to structural changes of the bulk. By contrast, those materials containing high-voltage redox couples such as $\text{Ni}^{2+}/\text{Ni}^{4+}$, $\text{Cu}^{2+}/\text{Cu}^{3+}$, and $\text{O}^{2-}/\text{O}^{0-}$, generally show much better air-stabilities, thanks to the higher energy barriers for chemical Na^+ extraction. Although it is found that the structural deterioration in moist air can be recovered by thermal treatments, the as-resulted increased cost for material storage is surely unfavorable. In this case, doping with Ni, Cu, and Li et al. are suggested as effective strategies to enhance the air-stability of Fe-based layered materials.^[53,158] Moreover, as mentioned before, coating with stable surface layers are also proposed to solve this problem.

4.5. Balance of Capacity, Cycling Life, and Cost

Although Fe-based layered cathodes for SIBs exhibit a maximum reversible capacity over 200 mAh g^{-1} , in most cases only 50%–70% of that can be stably output. Deep Na^+ extraction/insertion processing with high capacities always brings fast capacity fading. To gain better cycling stability, we normally have to limit the working voltage window at the expense of capacity or substitute Fe with other active TM elements. The introduction of Co and/or Ni would certainly boost the reversible capacity and energy density, however, resulting in concerns of cost again. Therefore, before the key problems of iron are well solved, the composition of the layered oxides should be carefully selected to approach a good balance of high capacity, long cycle life, and low cost, meeting the requests of practical utilizations. Among reported Fe-containing layered cathodes to date, Ni–Fe–Mn and Cu–Fe–Mn based materials and their derivatives (e.g., Ni–Cu–Fe–Mn, Ni–Cu–Fe–Mn–Ti based oxides) are suggested as the most promising candidates, which have been applied to develop commercial SIBs.^[159,160] In the near future, efforts can be devoted to optimize the composition of Fe-containing oxides

to achieve better performances and to further disclose the key issues of iron in great details so as to explore Fe-rich materials.

5. Summary

In summary, we have comprehensively reviewed the research history, recent progress and related key issues of Fe-based layered cathode materials for rechargeable SIBs. The electrochemical activities of $\text{Fe}^{3+/4+}$ redox couple in sodium layered oxides have offered new chance to develop Ni/Co free cathode materials for SIBs with combined merits of high capacity and low cost. The key problems of Fe-based layered oxides majorly lie in the migration of Fe ions from a transition metal layer to a sodium layer during deep Na^+ extraction, which leads to oxygen evolution, large polarization, unfavorable phase transition, hindered Na^+ diffusion, and fast capacity fading. Poor air-stability are also a serious issue that impede the practical utilizations of Fe-based layered cathodes. Cationic doping/substitution is the main and most promising method to overcome above-mentioned problems. Specially, coupling the merits of Fe and Mn to design Fe–Mn based layered oxides is an attractive research topic in consideration of the electrochemical performances and materials costs. Meanwhile, more in-depth investigations on Li/Fe substitution and Na-sites doping are strongly suggested as they have exhibited powerful effectiveness in stabilizing the host structure of several layered-type cathode materials. In addition, importing high-voltage redox couples such as Ni and Cu as well as surface modifications are also good approaches to improve the air-stability and practical utility of Fe-based layered materials. It should also be pointed out that, more efforts are still needed to solve the problems of Fe migration with less decrease of Fe content, to explore Fe-rich layered oxides.

Acknowledgements

This work was financially supported by Science and Technology Foundation of Guizhou Province (QKHZC[2020]2Y037).

Conflict of Interest

The authors declare no conflict of interest.

Keywords: cathode material · layered oxide · iron · sodium-ion battery

- [1] M. Armand, J. M. Tarascon, *Nature* **2008**, *451*, 652–657.
- [2] J. Y. Hwang, S. T. Myung, Y. K. Sun, *Chem. Soc. Rev.* **2017**, *46*, 3529–3614.
- [3] N. Yabuuchi, K. Kubota, M. Dahbi, S. Komaba, *Chem. Rev.* **2014**, *114*, 11636–11682.
- [4] C. Delmas, *Adv. Energy Mater.* **2018**, *8*, 1703137.
- [5] J. M. Tarascon, *Nat. Chem.* **2010**, *2*, 510.

- [6] J. M. Tarascon, M. Armand, *Materials for sustainable energy: a collection of peer-reviewed research and review articles from Nature Publishing Group*, Singapore: Macmillan and World Scientific, 2011, pp171–179.
- [7] T. Liu, Y. Zhang, Z. Jiang, X. Zeng, J. Ji, Z. Li, X. Gao, M. Sun, Z. Lin, M. Ling, J. Zheng, C. Liang, *Energy Environ. Sci.* **2019**, *12*, 1512–1533.
- [8] B. Dunn, H. Kamath, J.-M. Tarascon, *Science* **2011**, *334*, 928–935.
- [9] J. M. Tarascon, *Joule* **2020**, *4*, 1–5.
- [10] M. H. Han, E. Gonzalo, G. Singh, T. Rojo, *Energy Environ. Sci.* **2015**, *8*, 81–102.
- [11] H. Hou, C. E. Banks, M. Jing, Y. Zhang, X. Ji, *Adv. Mater.* **2015**, *27*, 7861–7866.
- [12] T. Rojo, Y.-S. Hu, M. Forsyth, X. Li, *Adv. Energy Mater.* **2018**, *8*, 1800880.
- [13] S. P. Ong, V. L. Chevrier, G. Hautier, A. Jain, C. Moore, S. Kim, X. Ma, G. Ceder, *Energy Environ. Sci.* **2011**, *4*, 3680.
- [14] C. Vaalma, D. Buchholz, M. Weil, S. Passerini, *Nat. Rev. Mater.* **2018**, *3*, 1–11.
- [15] K. M. Abraham, *ACS Energy Lett.* **2020**, *5*, 3544–3547.
- [16] G. J. May, A. Davidson, B. Monahov, *J. Energy Storage* **2018**, *15*, 145–157.
- [17] Y.R Liang, C.Z Zhao, H. Yuan, Y. Chen, W. C. Zhang, J.Q Huang, D. S. Yu, Y. L. Liu, M. M. Titirici, Y. L. Chueh, H. J. Yu, Q. Zhang, *InfoMat* **2019**, *1*, 6–32.
- [18] Y. Zhang, R. Zhang, Y. Huang, *Front. Chem.* **2019**, *7*, 335.
- [19] Y. Li, Y. Lu, C. Zhao, Y. S. Hu, M. M. Titirici, H. Li, X. Huang, L. Chen, *Energy Storage Mater.* **2017**, *7*, 130–151.
- [20] Y. P. Deng, Z. G. Wu, R. Liang, Y. Jiang, D. Luo, A. Yu, Z. Chen, *Adv. Funct. Mater.* **2019**, *29*, 1808522.
- [21] P. F. Wang, Y. You, Y. X. Yin, Y. G. Guo, *Adv. Energy Mater.* **2018**, *8*, 1701912.
- [22] Y. Xiao, Y. F. Zhu, S. Li, S. J. Tan, W. Ling, L. Peng, T. Q. Yang, L. D. Wang, X. D. Guo, Y. X. Yin, H. Zhang, Y. G. Guo, *Adv. Funct. Mater.* **2020**, *30*, 2001334.
- [23] K. Kubota, N. Yabuuchi, H. Yoshida, M. Dahbi, S. Komaba, *MRS Bull.* **2014**, *39*, 416–422.
- [24] M. Chen, Y. Zhang, G. Xing, Y. Tang, *Front. Chem.* **2020**, *8*, 152.
- [25] Y. Fang, J. Zhang, L. Xiao, X. Ai, Y. Cao, H. Yang, *Adv. Sci.* **2017**, *4*, 1600392.
- [26] Y. Niu, Y. Zhang, M. Xu, *J. Mater. Chem. A* **2019**, *7*, 15006–15025.
- [27] J. Qian, C. Wu, Y. Cao, Z. Ma, Y. Huang, X. Ai, H. Yang, *Adv. Energy Mater.* **2018**, *8*, 1702619.
- [28] B. Wang, Y. Han, X. Wang, N. Bahlawane, H. Pan, M. Yan, Y. Jiang, *iScience* **2018**, *3*, 110–133.
- [29] K. Kubota, S. Kumakura, Y. Yoda, K. Kuroki, S. Komaba, *Adv. Energy Mater.* **2018**, *8*, 1703415.
- [30] C. Zhao, Q. Wang, Z. Yao, J. Wang, B. Sánchez-Lengeling, F. Ding, X. Qi, Y. Lu, X. Bai, B. Li, H. Li, A. Aspuru-Guzik, X. Huang, C. Delmas, M. Wagemaker, L. Chen, Y. S. Hu, *Science* **2020**, *370*, 708–711.
- [31] A. Manthiram, *Nat. Commun.* **2020**, *11*, 1550.
- [32] H. Li, S. Liu, T. Yuan, B. Wang, P. Sheng, L. Xu, G. Zhao, H. Bai, X. Chen, Z. Chen, *Acta Phys. Chim. Sin.* **2020**, *36*.
- [33] M. Chen, Q. Liu, Z. Hu, Y. Zhang, G. Xing, Y. Tang, S. L. Chou, *Adv. Energy Mater.* **2020**, *10*, 2002244.
- [34] M. Chen, J. Xiao, W. Hua, Z. Hu, W. Wang, Q. Gu, Y. Tang, S. L. Chou, H. K. Liu, S. X. Dou, *Angew. Chem.* **2020**, *59*, 12076–12083.
- [35] N. Yabuuchi, S. Komaba, *Sci. Technol. Adv. Mater.* **2014**, *15*, 043501.
- [36] J. Kim, D. H. Seo, H. Kim, I. Park, J. K. Yoo, S. K. Jung, Y. U. Park, W. A. Goddard III, K. Kang, *Energy Environ. Sci.* **2015**, *8*, 540–545.
- [37] Y. Liu, N. Zhang, F. Wang, X. Liu, L. Jiao, L.-Z. Fan, *Adv. Funct. Mater.* **2018**, *28*, 1801917.
- [38] C. Li, X. Miao, W. Chu, P. Wu, D. G. Tong, *J. Mater. Chem. A* **2015**, *3*, 8265–8271.
- [39] B. L. Ellis, W. R. Makahnouk, Y. Makimura, K. Toghill, L. F. Nazar, *Nat. Mater.* **2007**, *6*, 749–753.
- [40] X. Deng, W. Shi, J. Sunarso, M. Liu, Z. Shao, *ACS Appl. Mater. Interfaces* **2017**, *9*, 16280–16287.
- [41] H. Kim, R. A. Shakoor, C. Park, S. Y. Lim, J.-S. Kim, Y. N. Jo, W. Cho, K. Miyasaka, R. Kahraman, Y. Jung, J. W. Choi, *Adv. Funct. Mater.* **2013**, *23*, 1147–1155.
- [42] P. Barpanda, G. Liu, C. D. Ling, M. Tamaru, M. Avdeev, S.-C. Chung, Y. Yamada, A. Yamada, *Chem. Mater.* **2013**, *25*, 3480–3487.
- [43] M. Chen, W. Hua, J. Xiao, D. Cortie, W. Chen, E. Wang, Z. Hu, Q. Gu, X. Wang, S. Indris, S. L. Chou, S. X. Dou, *Nat. Commun.* **2019**, *10*, 1480.
- [44] J. Song, L. Wang, Y. Lu, J. Liu, B. Guo, P. Xiao, J. J. Lee, X. Q. Yang, G. Henkelman, J. B. Goodenough, *J. Am. Chem. Soc.* **2015**, *137*, 2658–2664.

- [45] W. J. Li, S. L. Chou, J. Z. Wang, Y. M. Kang, J. L. Wang, Y. Liu, Q. F. Gu, H. K. Liu, S. X. Dou, *Chem. Mater.* **2015**, *27*, 1997–2003.
- [46] H. Fu, C. Liu, C. Zhang, W. Ma, K. Wang, Z. Li, X. Lu, G. Cao, *J. Mater. Chem. A* **2017**, *5*, 9604–9610.
- [47] P. Barpanda, G. Oyama, S. Nishimura, S. C. Chung, A. Yamada, *Nat. Commun.* **2014**, *5*, 4358.
- [48] G. Oyama, S. Nishimura, Y. Suzuki, M. Okubo, A. Yamada, *ChemElectroChem* **2015**, *2*, 1019–1023.
- [49] N. Yabuuchi, M. Kajiyama, J. Iwatake, H. Nishikawa, S. Hitomi, R. Okuyama, R. Usui, Y. Yamada, S. Komaba, *Nat. Mater.* **2012**, *11*, 512–517.
- [50] S. Y. Xu, X. Y. Wu, Y. M. Li, Y. S. Hu, L. Q. Chen, *Chin. Phys.* **2014**, *23*, 118202.
- [51] H. Yoshida, N. Yabuuchi, S. Komaba, *Electrochim. Commun.* **2013**, *34*, 60–63.
- [52] D. Kim, E. Lee, M. Slater, W. Lu, S. Rood, C. S. Johnson, *Electrochim. Commun.* **2012**, *18*, 66–69.
- [53] L. Mu, S. Xu, Y. Li, Y. S. Hu, H. Li, L. Chen, X. Huang, *Adv. Mater.* **2015**, *27*, 6928–6933.
- [54] C. Delmas, J.-J. Braconnier, C. Fouassier, P. Hagenmuller, *Solid State Ionics* **1981**, *3*, 165–169.
- [55] C. Fouassier, C. Delmas, P. Hagenmuller, *Mater. Res. Bull.* **1975**, *10*, 443–449.
- [56] A. Mendiboure, C. Delmas, P. Hagenmuller, *J. Solid State Chem.* **1985**, *57*, 323–331.
- [57] K. Du, J. Y. Zhou, G. R. Hu, H. C. Gao, Y.T Li, J. B. Goodenough, *Energy Environ. Sci.* **2016**, *9*, 2575–2577.
- [58] Q. Huang, J. Liu, L. Zhang, S. Xu, L. Chen, P. Wang, D. G. Ivey, W. Wei, *Nano Energy* **2018**, *44*, 336–344.
- [59] L. Shacklette, T. Jow, L. Townsend, *J. Electrochem. Soc.* **1988**, *135*, 2669.
- [60] N. A. Katcho, J. Carrasco, D. Saurel, E. Gonzalo, M. Han, F. Aguesse, T. Rojo, *Adv. Energy Mater.* **2017**, *7*, 1601477.
- [61] E. Talaei, V. Duffort, H. L. Smith, B. Fultz, L. F. Nazar, *Energy Environ. Sci.* **2015**, *8*, 2512–2523.
- [62] J. W. Somerville, A. Sobkowiak, N. Tapia-Ruiz, J. Billaud, J. G. Lozano, R. A. House, L. C. Gallington, T. Ericsson, L. Häggström, M. R. Roberts, U. Maitra, P. G. Bruce, *Energy Environ. Sci.* **2019**, *12*, 2223–2232.
- [63] P. F. Wang, Y. You, Y. X. Yin, Y. S. Wang, L. J. Wan, L. Gu, Y. G. Guo, *Angew. Chem.* **2016**, *55*, 7445–7449.
- [64] N. Yabuuchi, H. Yoshida, S. Komaba, *Electrochemistry* **2012**, *80*, 716–719.
- [65] S. Kikkawa, S. Miyazaki, M. Koizumi, *Mater. Res. Bull.* **1985**, *20*, 373–377.
- [66] S. Okada, Y. Takahashi, T. Kiyabu, T. Doi, J.-I. Yamaki, T. Nishida, *Meet. Abstr.* **2006**, MA2006-02, 201.
- [67] M. Hirayama, H. Tomita, K. Kubota, R. Kanno, *J. Power Sources* **2011**, *196*, 6809–6814.
- [68] Y. Takeda, K. Nakahara, M. Nishijima, N. Imanishi, O. Yamamoto, M. Takano, R. Kanno, *Mater. Res. Bull.* **1994**, *29*, 659–666.
- [69] J. Zhao, L. Zhao, N. Dimov, S. Okada, T. Nishida, *J. Electrochim. Soc.* **2013**, *160*, A3077-A3081.
- [70] E. Lee, D. E. Brown, E. E. Alp, Y. Ren, J. Lu, J.-J. Woo, C. S. Johnson, *Chem. Mater.* **2015**, *27*, 6755–6764.
- [71] D. Susanto, M. K. Cho, G. Ali, J.-Y. Kim, H. J. Chang, H.-S. Kim, K.-W. Nam, K. Y. Chung, *Chem. Mater.* **2019**, *31*, 3644–3651.
- [72] B. Silván, E. Gonzalo, L. Djuandhi, N. Sharma, F. Fauth, D. Saurel, *J. Mater. Chem. A* **2018**, *6*, 15132–15146.
- [73] Y. Li, Y. Gao, X. Wang, X. Shen, Q. Kong, R. Yu, G. Lu, Z. Wang, L. Chen, *Nano Energy* **2018**, *47*, 519–526.
- [74] X. Li, Y. Wang, D. Wu, L. Liu, S.-H. Bo, G. Ceder, *Chem. Mater.* **2016**, *28*, 6575–6583.
- [75] G. G. Eshetu, G. A. Elia, M. Armand, M. Forsyth, S. Komaba, T. Rojo, S. Passerini, *Adv. Energy Mater.* **2020**, *10*, 2000093.
- [76] C. Y. Yu, J. S. Park, H. G. Jung, K. Y. Chung, D. Aurbach, Y.-K. Sun, S.-T. Myung, *Energy Environ. Sci.* **2015**, *8*, 2019–2026.
- [77] Y. Wang, P. Cui, W. Zhu, Z. Feng, M. J. Vigeant, H. Demers, A. Guerfi, K. Zaghib, *J. Power Sources* **2019**, *435*, 226760.
- [78] J. Xu, Z. Han, K. Jiang, P. Bai, Y. Liang, X. Zhang, P. Wang, S. Guo, H. Zhou, *Small* **2020**, *16*, e1904388.
- [79] F. Kanamaru, H. Miyamoto, Y. Mimura, M. Koizumi, M. Shimada, S. Kume, S. Shin, *Mater. Res. Bull.* **1970**, *5*, 257–261.
- [80] Y. Fang, Z. Chen, L. Xiao, X. Ai, Y. Cao, H. Yang, *Small* **2018**, *14*, 1703116.
- [81] Q. Liu, Z. Hu, M. Chen, C. Zou, H. Jin, S. Wang, S. L. Chou, S. X. Dou, *Small* **2019**, *15*, e1805381.
- [82] N. Ortiz-Vitoriano, N. E. Drewett, E. Gonzalo, T. Rojo, *Energy Environ. Sci.* **2017**, *10*, 1051–1074.
- [83] J. Zhao, J. Xu, D. H. Lee, N. Dimov, Y. S. Meng, S. Okada, *J. Power Sources* **2014**, *264*, 235–239.
- [84] B. Mortemard de Boisse, D. Carlier, M. Guignard, C. Delmas, *J. Electrochem. Soc.* **2013**, *160*, A569-A574.
- [85] J. S. Thorne, R. A. Dunlap, M. N. Obrovac, *J. Electrochim. Soc.* **2012**, *160*, A361–A367.
- [86] G. Singh, B. Acebedo, M. C. Cabanas, D. Shanmukaraj, M. Armand, T. Rojo, *Electrochim. Commun.* **2013**, *37*, 61–63.
- [87] J. H. Jo, J. U. Choi, Y. J. Park, J. K. Ko, H. Yashiro, S.-T. Myung, *Energy Storage Mater.* **2020**, *32*, 281–289.
- [88] Y. B. Niu, Y. J. Guo, Y. X. Yin, S. Y. Zhang, T. Wang, P. Wang, S. Xin, Y. G. Guo, *Adv. Mater.* **2020**, *32*, e2001419.
- [89] B. Mortemard de Boisse, D. Carlier, M. Guignard, L. Bourgeois, C. Delmas, *Inorg. Chem.* **2014**, *53*, 11197–11205.
- [90] N. Sharma, M. H. Han, J. C. Pramudita, E. Gonzalo, H. E. A. Brand, T. Rojo, *J. Mater. Chem. A* **2015**, *3*, 21023–21038.
- [91] W. M. Dose, N. Sharma, J. C. Pramudita, J. A. Kimpton, E. Gonzalo, M. H. Han, T. Rojo, *Chem. Mater.* **2016**, *28*, 6342–6354.
- [92] G. Singh, J. M. Ld. Amo, M. Galceran, S. P. Villar, T. Rojo, *J. Mater. Chem. A* **2015**, *13*, 6954–6961.
- [93] S. Kumakura, Y. Tahara, K. Kubota, K. Chihara, S. Komaba, *Angew. Chem.* **2016**, *55*, 1–5.
- [94] W. K. Pang, S. Kalluri, V. K. Peterson, N. Sharma, J. Kimpton, B. Johannessen, H. K. Liu, S. X. Dou, Z. P. Guo, *Chem. Mater.* **2015**, *27*, 3150–3158.
- [95] S. Kalluri, K. H. Seng, W. K. Pang, Z. Guo, Z. Chen, H. K. Liu, S. X. Dou, *ACS Appl. Mater. Interfaces* **2014**, *6*, 8953–8958.
- [96] H. Zhu, K. T. Lee, G. T. Hitz, X. Han, Y. Li, J. Wan, S. Lacey, A. Cresce, K. Xu, E. Wachsman, L. Hu, *ACS Appl. Mater. Interfaces* **2014**, *6*, 4242–4247.
- [97] Y. Bai, L. Zhao, C. Wu, H. Li, Y. Li, F. Wu, *ACS Appl. Mater. Interfaces* **2016**, *8*, 2857–2865.
- [98] M. Li, D. L. Wood, Y. Bai, R. Essehl, M. R. Amin, C. Jafta, N. Muralidharan, J. Li, I. Belharouak, *ACS Appl. Mater. Interfaces* **2020**, *12*, 23951–23958.
- [99] E. Gonzalo, M. H. Han, J. M. López del Amo, B. Acebedo, M. Casas-Cabanas, T. Rojo, *J. Mater. Chem. A* **2014**, *2*, 18523–18530.
- [100] W. Zhao, Y. Tsuchiya, N. Yabuuchi, *Small Methods* **2018**, *3*, 1800032.
- [101] X. Lu, Y. Wang, P. Liu, L. Gu, Y. S. Hu, H. Li, G. P. Demopoulos, L. Chen, *Phys. Chem. Chem. Phys.* **2014**, *16*, 21946–21952.
- [102] M. H. Han, B. Acebedo, E. Gonzalo, P. S. Fontecoba, S. Clarke, D. Saurel, T. Rojo, *Electrochim. Acta* **2015**, *182*, 1029–1036.
- [103] N. Sharma, E. Gonzalo, J. C. Pramudita, M. H. Han, H. E. A. Brand, J. N. Hart, W. K. Pang, Z. Guo, T. Rojo, *Adv. Funct. Mater.* **2015**, *25*, 4994–5005.
- [104] B. V. Rami Reddy, R. Ravikumar, C. Nithya, S. Gopukumar, J. Mater. Chem. A **2015**, *3*, 18059–18063.
- [105] P. Vassilaras, X. Ma, X. Li, G. Ceder, *J. Electrochim. Soc.* **2012**, *160*, A207–A211.
- [106] X. Wang, G. Liu, T. Iwao, M. Okubo, A. Yamada, *J. Phys. Chem. C* **2014**, *118*, 2970–2976.
- [107] K. Kubota, T. Asari, H. Yoshida, N. Yaabuuchi, H. Shiiba, M. Nakayama, S. Komaba, *Adv. Funct. Mater.* **2016**, *26*, 6047–6059.
- [108] H. Yu, S. Guo, Y. Zhu, M. Ishida, H. Zhou, *Chem. Commun.* **2014**, *50*, 457–459.
- [109] J. S. Thorne, S. Chowdhury, R. A. Dunlap, M. N. Obrovac, *J. Electrochim. Soc.* **2014**, *161*, A1801–A1805.
- [110] M. Tamaru, X. Wang, M. Okubo, A. Yamada, *Electrochim. Commun.* **2013**, *33*, 23–26.
- [111] D. Yuan, X. Hu, J. Qian, F. Pei, F. Wu, R. Mao, X. Ai, H. Yang, Y. Cao, *Electrochim. Acta* **2014**, *116*, 300–305.
- [112] I. Hasa, D. Buchholz, S. Passerini, B. Scrosati, J. Hassoun, *Adv. Energy Mater.* **2014**, *4*, 1400083.
- [113] H. Wang, X.-Z. Liao, Y. Yang, X. Yan, Y.-S. He, Z.-F. Ma, *J. Electrochim. Soc.* **2016**, *163*, A565–A570.
- [114] Q. Zhang, Y. Huang, Y. Liu, S. Sun, K. Wang, Y. Li, X. Li, J. Han, Y. Huang, *Sci. China Mater.* **2017**, *60*, 629–636.
- [115] L. Sun, Y. Xie, X. Z. Liao, H. Wang, G. Tan, Z. Chen, Y. Ren, J. Gim, W. Tang, Y. S. He, K. Amine, Z. F. Ma, *Small* **2018**, *14*, e1704523.
- [116] Y. Sun, H. Wang, D. Meng, X. Li, X. Liao, H. Che, G. Cui, F. Yu, W. Yang, L. Li, Z.-F. Ma, *ACS Appl. Mater. Interfaces* **2021**, *4*, 2061–2067.
- [117] M. Jeong, H. Lee, J. Yoon, W.-S. Yoon, *J. Power Sources* **2019**, *439*, 227064.

- [118] M. Y. Naoaki Yabuuchi, Hiroaki Yoshida, Satoru Kuze, Shinichi Komaba, *J. Electrochem. Soc.* **2013**, *160*, A3131.
- [119] S. M. Oh, S. T. Myung, C. S. Yoon, J. Lu, J. Hassoun, B. Scrosati, K. Amine, Y. K. Sun, *Nano Lett.* **2014**, *14*, 1620–1626.
- [120] X. Qi, L. Liu, N. Song, F. Gao, K. Yang, Y. Lu, H. Yang, Y. S. Hu, Z. H. Cheng, L. Chen, *ACS Appl. Mater. Interfaces* **2017**, *9*, 40215–40223.
- [121] Q. Xinguo, W. Weigang, H. Yongsheng, *Energy SCI. Technol.* **2020**, *9*, 1396.
- [122] J. C. Kim, D. H. Kwon, J. H. Yang, H. Kim, S. H. Bo, L. Wu, H. Kim, D. H. Seo, T. Shi, J. Wang, Y. Zhu, G. Ceder, *Adv. Energy Mater.* **2020**, *10*, 2001151.
- [123] L. Liu, X. Li, S.-H. Bo, Y. Wang, H. Chen, N. Twu, D. Wu, G. Ceder, *Adv. Energy Mater.* **2015**, *5*, 1500944.
- [124] Y. H. Jung, A. S. Christiansen, R. E. Johnsen, P. Norby, D. K. Kim, *Adv. Funct. Mater.* **2015**, *25*, 3227–3237.
- [125] J. S. Thorne, R. A. Dunlap, M. N. Obrovac, *J. Electrochem. Soc.* **2014**, *161*, A2232–A2236.
- [126] E. Talaie, S. Y. Kim, N. Chen, L. F. Nazar, *Chem. Mater.* **2017**, *29*, 6684–6697.
- [127] Y. Li, Z. Yang, S. Xu, L. Mu, L. Gu, Y. S. Hu, H. Li, L. Chen, *Adv. Sci.* **2015**, *2*, 1500031.
- [128] S. Xu, J. Wu, E. Hu, Q. Li, J. Zhang, Y. Wang, E. Stavitski, L. Jiang, X. Rong, X. Yu, W. Yang, X. Q. Yang, L. Chen, Y.-S. Hu, *J. Mater. Chem. A* **2018**, *6*, 20795–20803.
- [129] Q. Shen, X. Zhao, Y. Liu, Y. Li, J. Zhang, N. Zhang, C. Yang, J. Chen, *Adv. Sci.* **2020**, *7*, 2002199.
- [130] X. Gao, F. Jiang, Y. Yang, Y. Zhang, G. Zou, H. Hou, Y. Hu, W. Sun, X. Ji, *ACS Appl. Mater. Interfaces* **2019**, *12*, 2432–2444.
- [131] J. Xu, J. Chen, K. Zhang, N. Li, L. Tao, C.-P. Wong, *Nano Energy* **2020**, *78*, 105142.
- [132] X. Gao, J. Chen, H. Liu, S. Yin, Y. Tian, X. Cao, G. Zou, H. Hou, W. Wei, L. Chen, X. Ji, *Chem. Eng. J.* **2021**, *406*, 126830.
- [133] Y. Zhang, S. Kim, G. Feng, Y. Wang, L. Liu, G. Ceder, X. Li, *J. Electrochem. Soc.* **2018**, *165*, A1184–A1192.
- [134] L. Yang, X. Li, J. Liu, S. Xiong, X. Ma, P. Liu, J. Bai, W. Xu, Y. Tang, Y. Y. Hu, M. Liu, H. Chen, *J. Am. Chem. Soc.* **2019**, *141*, 6680–6689.
- [135] Y. Kee, N. Dimov, S. Champet, D. H. Gregory, S. Okada, *Ionics* **2016**, *22*, 2245–2248.
- [136] H. Wang, R. Gao, Z. Li, L. Sun, Z. Hu, X. Liu, *Inorg. Chem.* **2018**, *57*, 5249–5257.
- [137] L. Zhang, T. Yuan, L. Soule, H. Sun, Y. Pang, J. Yang, S. Zheng, *ACS Appl. Mater. Interfaces* **2020**, *3*, 3770–3778.
- [138] D. Zhou, W. Huang, X. Lv, F. Zhao, *J. Power Sources* **2019**, *421*, 147–155.
- [139] J. Yang, A. E. Maughan, G. Teeter, B. J. Tremolet de Villers, S. M. Bak, S. D. Han, *ChemSusChem* **2020**, *13*, 5972–5982.
- [140] Q. C. Wang, J. K. Meng, X. Y. Yue, Q. Q. Qiu, Y. Song, X. J. Wu, Z. W. Fu, Y. Y. Xia, Z. Shadike, J. Wu, X. Q. Yang, Y. N. Zhou, *J. Am. Chem. Soc.* **2019**, *141*, 840–848.
- [141] Y. Huang, Z. Yan, W. Luo, Z. Hu, G. Liu, L. Zhang, X. Yang, M. Ou, W. Liu, L. Huang, H. Lin, C. T. Chen, J. Luo, S. Li, J. Han, S. Chou, Y. Huang, *Energy Storage Mater.* **2020**, *29*, 182–189.
- [142] J. Y. Hwang, J. Kim, T. Y. Yu, Y. K. Sun, *Adv. Energy Mater.* **2019**, *9*, 1803346.
- [143] Y. J. Park, J. U. Choi, J. H. Jo, C. H. Jo, J. Kim, S. T. Myung, *Adv. Funct. Mater.* **2019**, *29*, 1901912.
- [144] J. U. Choi, J. H. Jo, Y. J. Park, K. S. Lee, S. T. Myung, *Adv. Energy Mater.* **2020**, *10*, 2001346.
- [145] J. U. Choi, Y. J. Park, J. H. Jo, L. Y. Kuo, P. Kaghazchi, S. T. Myung, *ACS Appl. Mater. Interfaces* **2018**, *10*, 40978–40984.
- [146] J. U. Choi, C. S. Yoon, Q. Zhang, P. Kaghazchi, Y. H. Jung, K. S. Lee, D. C. Ahn, Y. K. Sun, S. T. Myung, *J. Mater. Chem. A* **2019**, *7*, 202–211.
- [147] J. Wang, X. He, D. Zhou, F. Schappacher, X. Zhang, H. Liu, M. C. Stan, X. Cao, R. Kloepsch, M. S. Sofy, G. Schumacher, J. Li, *J. Mater. Chem. A* **2016**, *4*, 3431–3437.
- [148] X. Li, D. Wu, Y. N. Zhou, L. Liu, X. Q. Yang, G. Ceder, *Electrochem. Commun.* **2014**, *49*, 51–54.
- [149] S. M. Oh, S.-T. Myung, J. Y. Hwang, B. Scrosati, K. Amine, Y.-K. Sun, *Chem. Mater.* **2014**, *26*, 6165–6171.
- [150] Y. You, S. Xin, H. Y. Asl, W. Li, P. F. Wang, Y.-G. Guo, A. Manthiram, *Chem* **2018**, *4*, 2124–2139.
- [151] C. Zhao, F. Ding, Y. Lu, L. Chen, Y. S. Hu, *Angew. Chem.* **2020**, *59*, 264–269.
- [152] M. Linqin, Q. Xinguo, H. Yongsheng, L. Hong, C. Liquan, H. Xuejie, *Energy Technol.* **2016**, *5*, 324.
- [153] S. Chu, C. Zhang, H. Xu, S. Guo, P. Wang, H. Zhou, *Angew. Chem. Int. Ed.* **2021**, *60*, 13366–13371.
- [154] C. Wang, L. Liu, S. Zhao, Y. Liu, Y. Yang, H. Yu, S. Lee, G. H. Lee, Y. M. Kang, R. Liu, F. Li, J. Chen, *Nat. Commun.* **2021**, *12*, 2256.
- [155] A. E. Bocquet, A. Fujimori, T. Mizokawa, T. Saitoh, H. Namatame, S. Suga, N. Kimizuka, Y. Takeda, M. Takano, *Phys. Rev. B* **1992**, *45*, 1561–1570.
- [156] V. Duffort, E. Talaie, R. Black, L. F. Nazar, *Chem. Mater.* **2015**, *27*, 2515–2524.
- [157] W. Zuo, J. Qiu, X. Liu, F. Ren, H. Liu, H. He, C. Luo, J. Li, G. F. Ortiz, H. Duan, J. Liu, M. S. Wang, Y. Li, R. Fu, Y. Yang, *Nat. Commun.* **2020**, *11*, 3544.
- [158] H. R. Yao, P. F. Wang, Y. Gong, J. Zhang, X. Yu, L. Gu, C. OuYang, Y. X. Yin, E. Hu, X. Q. Yang, E. Stavitski, Y. G. Guo, L. J. Wan, *J. Am. Chem. Soc.* **2017**, *139*, 8440–8443.
- [159] R. Usiskin, Y. Lu, J. Popovic, M. Law, P. Balaya, Y.-S. Hu, J. Maier, *Nat. Rev. Mater.* **2021**.
- [160] A. Tripathi, A. Rudola, S. R. Gajjela, S. Xi, P. Balaya, *J. Mater. Chem. A* **2019**, *7*, 25944–25960.

Manuscript received: May 16, 2021

Revised manuscript received: August 9, 2021

Version of record online: August 23, 2021